Materials Today 97 (2026) 103349

Contents lists available at ScienceDirect

Materials Today

journal homepage: www.elsevier.com/locate/mattod

Site specific porosity-thermal performance correlations in neutron irradiated U-10Zr fuel

Anthony A. Harrup [a,b], Riley Moeykens [a,b], Michael Drakopoulos [c], Nghia T. Vo [c], Jana Howard [d], Colby B. Jensen [d], Tiankai Yao [d,*], Ericmoore Jossou [a,b,e,**]

[a] Materials in Extreme Environments Laboratory, Massachusetts Institute of Technology (MIT), 77 Massachusetts Ave., Cambridge, MA 02139, USA
[b] Department of Nuclear Science and Engineering, Massachusetts Institute of Technology (MIT), Cambridge, MA, USA
[c] Brookhaven National Laboratory, National Synchrotron Light Source II, Upton, NY 11973, USA
[d] Idaho National Laboratory, Idaho Falls, ID 83415, USA
[e] Department of Electrical Engineering and Computer Science, Massachusetts Institute of Technology (MIT), Cambridge, MA 02139, USA

ARTICLE INFO

Keywords:
U-10Zr
Synchrotron micro-XCT
Nuclear fuel
Porosity
FCCI

ABSTRACT

We present a site-specific three-dimensional analysis of porosity evolution in neutron-irradiated U–10Zr metallic fuel using high-resolution synchrotron X-ray tomography. Focused ion beam cubic lift-outs from four radial positions—fuel center, middle, edge, and fuel-cladding interaction (FCCI) zones—were imaged, reconstructed, and segmented to quantify pore volume, density, morphology, and pore connectivity. Porosity increased modestly from 5.5% at the center to 10.5% at the edge, yet pore number density increased by over two orders of magnitude in the fuel portion near the FCCI interface (from 4.8×10^4 to 6.0×10^6 pores/mm^3). Morphological classification revealed a progression from small spherical pores at the center to equiaxed and tortuous networks at the periphery, with enhanced orientation along the radial direction. Connectivity and permeability analysis reveal that the FCCI region maintains dense, highly interconnected pores despite a moderate volume fraction, enabling rapid fission gas transport and lanthanide migration. Effective thermal conductivity models incorporating sodium logging confirm that these site-specific pore features critically influenced heat transport during reactor irradiation. These findings demonstrate that pore topology—not just porosity fraction—controls thermal performance and thermal pathways in U–10Zr fuels, impacting fuel thermal performance in a reactor.

Introduction

Uranium–10 weight percent zirconium (U–10Zr) is a leading candidate for advanced sodium-cooled fast reactor fuels due to its high uranium density, favorable thermal conductivity, and established performance under irradiation. Historically, more than 14,000 U–10Zr fuel rods have been irradiated in test reactors such as Experimental Breeder Reactor-II (EBR-II) and the Fast Flux Test Facility (FFTF), with some achieving burn ups almost 20 at.% [1]. This empirical record has enabled U–10Zr as a reference metallic fuel in the U.S. fast reactor program [2].

Despite the proven track record of U-10Zr, phenomena such as phase evolution, pore formation, and elemental redistribution remain poorly understood. To address these gaps, recent studies have applied advanced microscopy and tomography approaches. Recent studies, however, have leveraged advanced characterization techniques to gain new insights into the complex microstructural evolution of U–10Zr during irradiation. Salvato et al. used transmission electron microscopy (TEM) to identify three concentric zones formed due to zirconium redistribution: a central Zr-rich region (Zone 1), an intermediate Zr-depleted region (Zone 2), and an outer region with moderate Zr content (Zone 3). Each zone exhibits distinct microstructural features with regards to phase segregation, pore morphology, and solid fission product behavior [3]. In addition, TEM analyses revealed the formation of fine-scale δ-UZr$_2$, γ_2, and α-U phases, as well as complex porosity and lanthanide accumulation near grain boundaries and fuel-cladding interface.

Extensive characterization of fresh and irradiated U–10Zr fuels has been carried out using SEM, TEM, atom probe tomography and related focused ion beam (FIB) techniques [3–9]. These studies have revealed distinct radial redistribution zones, nanoscale phase separation—

* Corresponding author.
** Corresponding author at: Department of Nuclear Science and Engineering, Massachusetts Institute of Technology (MIT), Cambridge, MA, USA.
E-mail addresses: Tiankai.Yao@inl.gov (T. Yao), ejossou@mit.edu (E. Jossou).

https://doi.org/10.1016/j.mattod.2026.103349
Received 8 December 2025; Received in revised form 9 February 2026; Accepted 13 April 2026
Available online 5 May 2026

including γ_2, α-U, δ-UZr_2, and ω-UZr_2—and significant accumulation of fission products such as lanthanides, Ba–Te, and Cs–I compounds inside pores and at the interface. TEM analyses have also uncovered spinodal decomposition and compositional gradients that arise under irradiation and thermal cycling [5]. Although these methods are essential for phase identification, grain morphology, and chemical mapping, they are inherently limited in spatial resolution, sampling volume, and their ability to resolve 3D pore connectivity and topology across extended fuel regions, which is important for determining the effective thermal conductivity. Moreover, such techniques provide only localized insight into fuel-cladding chemical interactions (FCCI), including constituent interdiffusion and reaction layer formation, which evolve heterogeneously along the fuel length. Consequently, volumetric techniques such as synchrotron X-ray computed tomography (XCT) are increasingly needed to bridge the gap and enable non-destructive, depth-resolved analysis of porosity and constituent redistribution, and FCCI behavior over representative volumes of metallic fuels.

Synchrotron-based X-ray micro-computed tomography (micro-CT) has been widely applied to investigate fracture and porosity networks across a broad range of material systems, including geological media and fractured sandstones [10,11] as well as metallic and aerospace alloys during solidification [12]. More recently, these techniques have been extended to nuclear fuels, enabling three-dimensional, site-specific characterization of porosity and phase distributions in neutron-irradiated U–10Zr [7].

While prior studies have largely focused on the intermediate redistribution zone, where Zr depletion is most pronounced, the broader spatial variability of fuel behavior across the full cross-section remains underexplored. In this work, we extend XCT-based characterization to encompass all four key radial regions of the irradiated U–10Zr fuel, following the zone classification defined by Yao et al. which includes: (a) Zone 1: Zr-rich central region (U ~30–35 wt% Zr), (b) Zone 2: Zr-depleted intermediate region (U ~4 wt% Zr), (c) Zone 3: Outer region with moderate Zr content (U ~10 wt% Zr), (d) Zone 4: FCCI zone, where intermetallic phases and lanthanide fission products accumulate near the HT-9 cladding interface [13]. This classification is shown in Fig. 1 and sample for the measurements for the work were taken from each zone.

By combining high-resolution XCT with site-specific segmentation and porosity quantification, this study provides a comprehensive 3D view of pore distribution, connectivity, and microstructural heterogeneity across the fuel radius. In addition to offering new insights into the mechanisms that govern swelling, Zr migration, and FCCI in metallic fuels, the analysis also enables direct evaluation of how pore morphology and connectivity influence effective thermal conductivity across the fuel element. Extensive historical data exists [14], yet modern 3D imaging provides new insights into its behavior under irradiation and complex thermal gradients.

Materials and methods

Materials and liftouts for XCT

Each FIB lift-out represents a site-specific microstructural volume extracted from a well-defined radial zone rather than a statistically exhaustive sample of the entire fuel cross-section. While the limited volume precludes full statistical averaging, the observed pore morphologies, connectivity trends, and radial evolution are consistent with independent SEM- and TEM-based studies of irradiated U–10Zr fuels reported in the literature. The size of the analyzed volumes is constrained by radiological safety and handling requirements associated with highly irradiated fuel, which limit the feasible specimen dimensions for synchrotron-based tomography. Nevertheless, the agreement across techniques and length scales supports that the extracted volumes capture representative local pore characteristics of their respective radial regions.

Table 1
Synchrotron X-ray parameters at the high energy X-ray beamline for X-ray Computed Tomography imaging of U-10Zr.

Parameter	Value
X-ray energy	50 keV
Pixel size	0.65 μm
Voxel size	0.65 μm × 0.65 μm × 0.65 μm
Number of projections	1801
Rotation range	180°
Exposure time per frame	500 ms
Beamline	NSLS-II (HEX 27ID)

The material analyzed in this study is U-10 wt%Zr metallic fuel, enriched to 32.4% U-235, irradiated in the Fast Flux Test Facility (FFTF) as part of the MFF-3 experiment [14]. The fuel setup consisted of an assembly of 169 fuel pins, each approximately 91.4 cm in length and containing 2–4 fuel slugs produced by counter-gravity vacuum casting that reached a peak assembly burnup of 15.2 at.%.

The samples were extracted from MFF3 pin #193114 at an axial position of $x/L = 0.44$, where x is the distance from the bottom and R the total pin radius. The fuel cladding material is HT9 martensitic steel with a nominal composition of Fe–12Cr–1Mo–0.5W–0.5V–0.5Ni–0.2C–0.25Si–0.2Mn (wt.%) [3,15]. The four specimens, designated as MNT54C 1–4, were cut by focused ion beam (FIB) lift-out technique at the Irradiated Materials Characterization Laboratory (IMCL). Each cube measures approximately 50 μm per side and was taken from one of four radial positions: (1) the fuel center, (2) one-third radial depth, (3) the fuel edge, and (4) the fuel-cladding interface. These locations were selected to capture the characteristic microstructural gradients developed in high-burnup U–10Zr fuels [3].

Each liftout sample was welded to the tip of an alumina (Al_2O_3) rod of diameter 0.5 mm using platinum. The mounted samples were then enclosed in a double-layered quartz tube system, which serves as containment and complies with the radiological and safety requirements at NSLS-II. This system consists of two quartz tubes with different diameters: the outer tube has an outer diameter (OD) of 2.1 mm and an inner diameter (ID) of 1.9 mm, while the inner tube has an OD of 1.9 mm and an ID of 1.7 mm. The tubes were sealed with an alumina-based adhesive that also provides structural integrity.

Potential artifacts from focused ion beam (FIB) preparation were mitigated by restricting all quantitative pore analyses to interior subvolumes of each lift-out, excluding voxels near external surfaces. This conservative approach avoids possible ion-beam-affected regions such as redeposition or curtaining. The analyzed pore features are micrometer-scale and consistent with independent SEM and TEM observations of irradiated U–10Zr fuels reported in the literature, indicating that FIB preparation does not influence the conclusions of this study.

Imaging and data processing

The X-ray computed tomography was carried out at the HEX beamline [16], National Synchrotron Light Source II (NSLS-II), Brookhaven National Laboratory (BNL), using an X-ray beam with an energy of 50 keV. The effective voxel size was 0.65 μm. A total of 1801 projections were acquired over 180°, with an exposure time of 500 ms per projection. The experimental details are summarized in Table 1.

The reconstruction of the collected radiographs was performed at NSLS-II using the Algotom software [17] and Brookhaven National Lab's computer cluster. The reconstruction was performed using a processing pipeline that includes a flat field correction, ring artifact removal [18], and the filtered back-projection method. The reconstructed images were converted to 16-bit images.

The reconstructed 3D volumes were segmented using ilastik, a Python based random forest software [19] as well as other classical methods such as 1D and 4-D k-means clustering. After segmentation,

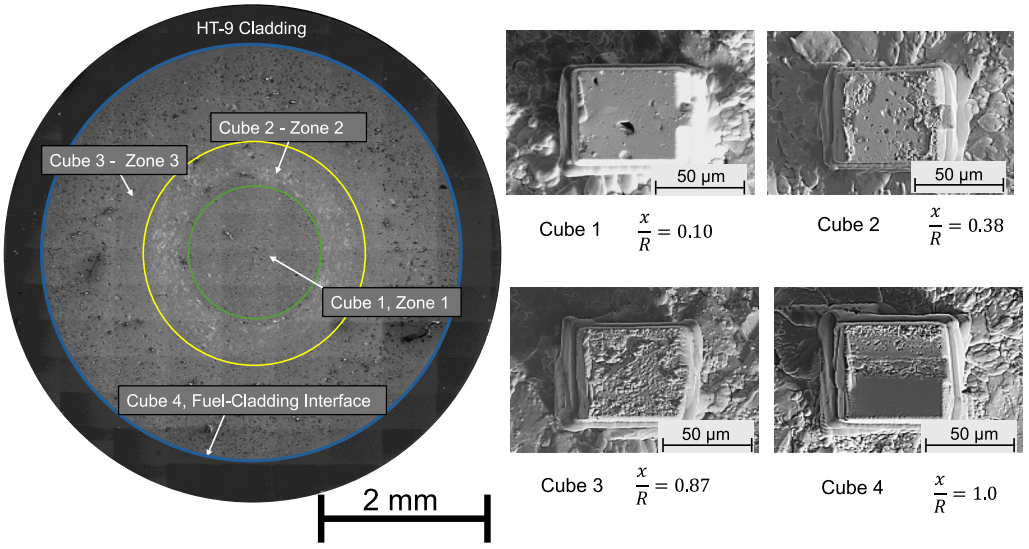

Fig. 1. Left: Cross-sectional X-ray image of the irradiated fuel pin showing the locations where focused ion beam (FIB) liftouts were performed. Each labeled region corresponds to one of four extracted cubic samples (Cubes 1–4), spanning the fuel center to the fuel-cladding interface. **Right**: Scanning electron microscopy (SEM) images of the liftouts are mounted on an alumina rod. The dimensionless parameter $\frac{x}{R}$ denotes the normalized radial position of each cube, where x is the distance from the center and R is the total radius.

the segmented volumes were analyzed using FIJI (ImageJ) software, including the 3D analysis plugin [20]. Segmentation accuracy was assessed through a combination of visual inspection and morphological consistency checks. Segmented pore volumes were systematically cross-validated against raw grayscale slices in multiple orthogonal planes to ensure correct phase assignment and boundary detection. In addition, extracted pore size, shape, and connectivity distributions were verified to be physically consistent with known irradiation-induced porosity characteristics of U–10Zr reported from independent SEM- and TEM-based studies. This multi-step verification ensured that segmentation artifacts did not influence the quantitative pore topology analysis. The 3D analyses were performed using a 26-voxel connectivity and a minimum threshold of 6 voxels. All 3D renderings were performed using Python, skimage, matplotlib, and pyvista packages. Fig. 2 shows the 3D views of the reconstructed 3D volumes. The bottom view shows the 3D rendering of the pores, created using a marching cube algorithm and 3D smoothing with 5 iterations.

Additionally, Energy-dispersive X-ray spectroscopy (EDS) was performed at an accelerating voltage of 20.0 kV, with a tilt angle of 0.0°, and a working distance of 43.0 mm. The image and EDS was collected at a magnification of 5007×, and a dwell time of 200 μs. The scans were performed in Boise State University at the Microscopy and Characterization Suite (MaCS).

Results and discussion

Porosity analysis

The segmented porosity was initially measured in terms of volume, where the percentage porosity can be calculated as follows:

$$\text{Porosity } (\%) = \frac{V_{\text{pore}}}{V_{\text{matrix}} + V_{\text{pore}}} \times 100 \quad (1)$$

where the volume of the porosity, V_{pore}, and the volume of the matrix, V_{matrix}, are expressed in voxels throughout the 3D reconstructed volume. The measured porosity values and corresponding volumetric pore densities for each radial region are summarized in Table 2.

Each individual pore was later labeled and its volume estimated using the marching cubes algorithm [21]. The 3D volumes reveal a distinct radial evolution in porosity volume fraction, as shown in Fig. 2. Starting from the center of the fuel (Zone 1), pores appear small, isolated, and spherical. This morphology is consistent with nucleation in Zr-rich matrices, particularly within the γ_2 and $\delta - UZr_2$ phases, which are commonly stabilized in the inner regions of the fuel due to Zr redistribution during irradiation [7,22].

Table 2
Measured porosity and pore density distribution across different regions of the U-10Zr fuel.

Region	Porosity volume (%)	Volumetric pore density (pores/mm^3)
Center	5.50 ± 0.2	4.8×10^4
Zr depleted zone (middle)	7.00 ± 0.3	5.2×10^4
Fuel periphery	10.50 ± 0.4	3.0×10^5
FCCI zone	6.62 ± 0.3	6.0×10^6
Wastage zone	7.40 ± 0.3	1.6×10^6

As the radial position increases (Zones 2 and 3), pores evolve into equiaxed and eventually complex geometries. These changes are due to the temperature gradient, irradiation phase changes, overpressurized gas bubbles which form cavities, and coalescence mechanisms of large and small pores, in agreement with prior SEM segmentation studies [23]. The intermediate regions are notably depleted in zirconium, dominated by α-U or distorted α/β-U phases, which allow for more unconstrained pore expansion [4,24]. This porosity progression is further supported by the increasing volume fraction of segmented pores toward the edge, as shown in Fig. 4.

The porosity increases from an average of ~5.5% in the central region to over 10.5% at the edge and even higher near the fuel-cladding interface, where pore coalescence and secondary phase transformations are most pronounced. These findings are consistent with 3D image-based quantifications in irradiated U–10Zr fuel [7,25] (see Table 2).

Pore morphological evolution and classification

Each individual pore was morphologically classified into spherical, equiaxed, or complex (tortuous) categories. In U–10Zr, pores arise primarily from the accumulation of fission gases and solid fission products during irradiation. Classical pore-growth theory suggests that newly formed pores are expected to nucleate with an approximately spherical geometry, as surface-energy minimization dominates at early stages of

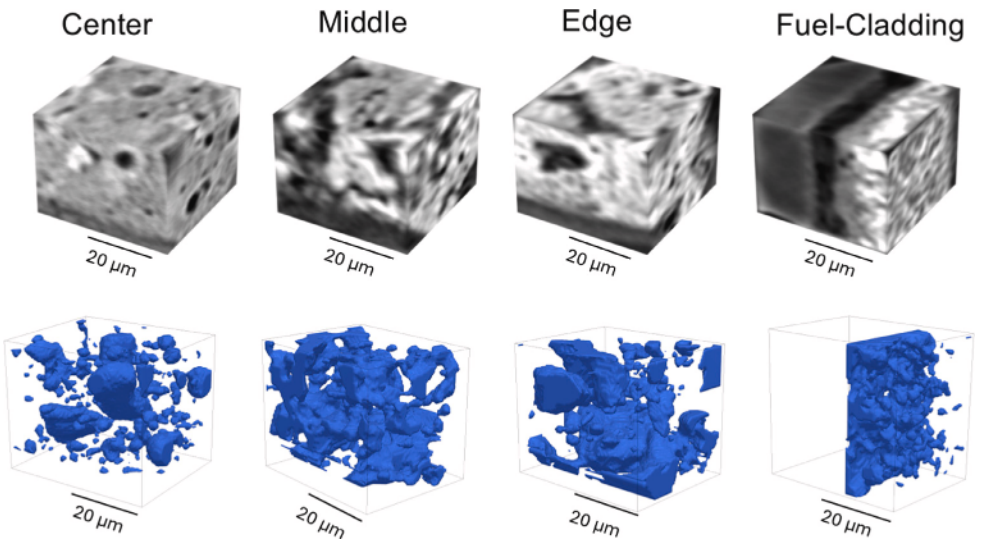

Fig. 2. 3D reconstructed microstructure (top row) and segmented porosity (bottom row) from X-ray tomography of U-10Zr fuel samples extracted at increasing radial distances: Center, Middle, Edge, and Fuel-Cladding interface. Each cube represents a 50 μm field of view. Segmented pore volumes (in blue) reveal changes in pore morphology and connectivity from the fuel center to the outer cladding interface, where larger, more interconnected porosity is observed near the edge and cladding.

formation [26]. However, in irradiated U–Zr systems, the subsequent evolution of these pores may not be solely determined by gas pressure. Instead, it is plausible that their growth and shape transitions are influenced by the local elastic and crystallographic environment of the surrounding phases, which can vary significantly across the fuel radius. Stiffer, Zr-rich δ-UZr_2 lamellae could restrict pore deformation, whereas pores embedded within more compliant U-rich α/γ_2 matrices may experience reduced mechanical constraint, enabling elongation, coalescence, and the emergence of tortuous, interconnected morphologies. This hypothesis is consistent with irradiation-driven transport mechanisms and microstructural rearrangements observed under strong thermal gradients [27], although the quantitative contribution of each factor such as elasticity, crystallography, and fission-product chemistry remains an open question that warrants further investigation.

To classify pore morphology, each pore is approximated as an ellipsoid with the same volume and principal moments of inertia (I_{xx}, I_{yy}, I_{zz}), as proposed by Fang et al. [28]. The following geometric parameters are computed such that the sphericity index (Ω_3) is calculated:

$$\Omega_3 = \frac{A}{\left(\pi^{\frac{1}{3}}(6V)^{\frac{2}{3}}\right)}$$

where A is the surface area and V is the volume of the pore. Meanwhile, the flatness (F) metric is calculated using:

$$F = \frac{b}{c}$$

And finally, the elongation (E) metric is computed using the relationship:

$$E = \frac{2a}{b+c}$$

where $a \geq b \geq c$ are the semi-axes of the best-fit ellipsoid derived from the inertia tensor. Based on these parameters, pores are classified using the threshold in Table 3.

Using this classification, pores are grouped by size and geometry, illustrating their evolution through a classical void growth mechanism. The corresponding morphology distributions across radial regions are summarized in Table 4, showing a clear transition from spherical to increasingly complex pore structures. Pores initially nucleate with a near-spherical morphology and, as they coarsen, evolve toward configurations that minimize interfacial energy. This behavior is analogous

Table 3
Classification scheme for pore shape based on elongation (E), flatness (F), and sphericity index (Ω_3).

Shape	E	F	Ω_3
Spherical	–	–	$\Omega_3 < 1.5$
Equiaxed	< 4	< 4	$1.5 \leq \Omega_3 < 2.5$
Rod	≥ 4	< 4	$1.5 \leq \Omega_3 < 2.5$
Sheet	–	≥ 4	$1.5 \leq \Omega_3 < 2.5$
Complex	–	–	$\Omega_3 \geq 2.5$

to Ostwald ripening, where smaller features dissolve and contribute to the growth of larger ones, reducing the overall surface energy of the system. The observed coarsening and increasing shape anisotropy along the radial direction suggest a temperature-driven mechanism, in which higher-temperature regions suppress coalescence, while cooler outer regions promote pore elongation and connectivity [13].

Based on the segmentation of SEM images, Xu et al. [22] categorized pores by size: small (area $\leq$ 32 μm^2), intermediate (32–205 μm^2), and large ($>$ 205 μm^2). Their analysis revealed increasing total porosity from the fuel center to the periphery, with small pores contributing consistently across the radius, and large pores becoming dominant in outer zones. Notably, porosity from large pores decreased near the cladding interface, potentially mitigating FCCI by limiting lanthanide transport pathways. These trends provide a benchmark for assessing pore evolution and spatial distribution in U–Zr fuels under irradiation.

Pore classification by morphology and orientation reveals further insight into the radial fuel behavior. Fig. 3 illustrates that the inner region (Zone 1) is dominated by small, round, and discrete pores, with minimal orientation preference. These are indicative of early-stage nucleation, consistent with isotropic swelling within Zr-rich zones [22].

Moving into Zone 2 ($0.32 < R < 0.48$), equiaxed and intermediate pores become dominant. The Zr content here is the lowest [7], and the matrix is structurally more compliant, facilitating anisotropic growth. As shown in Fig. 4, a transition toward a preferential 90° alignment becomes evident in Zone 3 and is pronounced at the edge. This angular shift implies radial expansion and suggests a preferred direction of migration for fission gases. Similar orientation-dependent pore migration has been linked to lanthanide redistribution and thermal gradient-driven flux [23].

Interestingly, Zone 4 (FCCI region) reverts to a Zr-rich phase while retaining a high fraction of complex, tortuous pores. This contra-

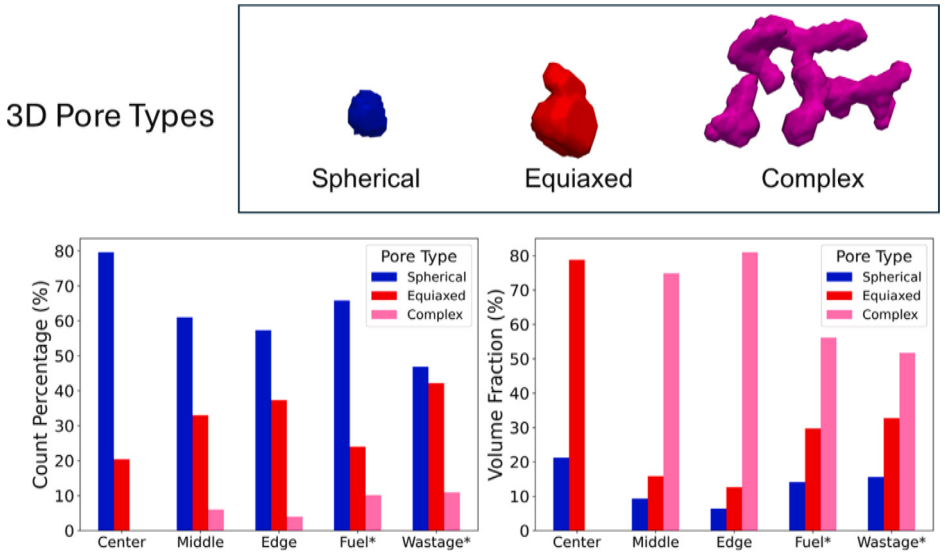

Fig. 3. Classification and distribution of 3D pore morphologies identified in U–10Zr fuel samples. **(Top)** Representative 3D renderings of the three main pore types based on shape descriptors: **Spherical** (blue), **Equiaxed** (red), and **Complex** (magenta). **(Bottom)** Count and volume percentage of each pore type across different sample regions: Center, Middle, Edge, Fuel and Wastage. Fuel* and Wastage* refer to the Fuel-Cladding interfacial zone.

Table 4
Percentage of pores within each angle range by classification, including overall distribution.

Classification	0–30°	30–60°	60–90°
Complex	28.57%	28.57%	42.86%
Equiaxed	20.00%	24.00%	56.00%
Spherical	34.48%	17.24%	48.28%
All pores	27.87%	21.31%	50.82%

diction—Zr-rich but morphologically advanced—may be explained by high local temperatures and stress-assisted interdiffusion [4,29]. Such conditions promote lanthanide condensation and the development of low-melting intermetallics, even in environments typically thought to suppress pore evolution (see Table 4).

The orientation of the pore was determined by computing the angle θ between the major principal axis $\vec{v}_{I1}$, which corresponds to the most significant moment of inertia, and the XY plane, which represents the moment cross-section of the fuel pin. If the angle is 0, it means that the pore is oriented towards the height of the fuel pin; meanwhile, if the angle is close to 90°, it implies that it is oriented towards the radius. This was calculated as follows:

$$\theta = \cos^{-1}\left(\frac{|\vec{v}_{I1}\cdot\hat{z}|}{\|\vec{v}_{I1}\|}\right) = \cos^{-1}\left(\frac{|v_z|}{\sqrt{v_x^2+v_y^2+v_z^2}}\right) \quad (2)$$

where $\vec{v}_{I1} = (v_x, v_y, v_z)$ is the direction vector of the principal axis I_1, and $\hat{z} = (0,0,1)$ is the normal vector to the XY plane. The use of the absolute value ensures that the angle is constrained between 0° (axis aligned with Z) and 90° (axis fully within the XY plane).

Pore connectivity and interconnection

To quantify 3D pore connectivity in the tomographic volumes, we developed a Python-based pipeline incorporating image segmentation, centroid extraction, and network graph analysis. The raw volumetric data were binarized by thresholding, identifying pore voxels. A Euclidean distance transform was applied to the binary mask, and local maxima were detected to initialize watershed segmentation, thereby assigning unique labels to each individual pore. Pore centroids were computed in voxel coordinates and converted to physical units using the voxel size $s = 0.65\,\mu\text{m}$.

To evaluate geometric connectivity, the pairwise Euclidean distance between centroids $\mathbf{c}_i$ and $\mathbf{c}_j$ was computed as:

$$d_{ij} = \|\mathbf{c}_i - \mathbf{c}_j\|_2$$

An adjacency matrix A was constructed using a distance threshold d_{th} such that:

$$A_{ij} = \begin{cases} 1 & \text{if } d_{ij} < d_{\text{th}} \text{ and } i \neq j \\ 0 & \text{otherwise} \end{cases}$$

From this matrix, an undirected graph $G = (V, E)$ was created, where nodes represent pores and edges represent pairwise connectivity under the threshold criterion. The connectivity was assessed across a range of distance thresholds (d_{th}) defined as $d_{\text{th}} \in [0\,\mu\text{m}, 12.5\,\mu\text{m}]$, with a step size of 0.5 µm. For each d_{th}, the following metrics were computed: (a) f_{largest}, the fraction of pores in the largest connected component, (b) f_{isolated}, the fraction of pores with no connections, and (c) f_{volume}, the cumulative volume fraction of all pores in the largest cluster. The cumulative connected volume fraction was calculated as:

$$f_{\text{volume}} = \frac{V_{\text{connected}}}{V_{\text{total}}}$$

where $V_{\text{connected}}$ is the sum of voxels associated with labels in the connected component, and V_{total} is the total pore volume in the image.

Fig. 4 shows that pores evolve from small, nearly spherical shapes at the center to equiaxed and more tortuous morphologies toward the edge/FCCI regions, with major axes increasingly aligned toward ~90° (radial direction along the temperature gradient during in reactor fuel operation). This progressive alignment toward 90° (radial direction) is consistent with outward heat flow during irradiation, which induces a strong radial thermal gradient that biases pore growth and migration toward the cooler periphery [23,30] This morphological/orientational shift shortens inter-pore path lengths and raises the likelihood that local clusters merge into system-spanning routes, amplifying the connectivity trends quantified in Fig. 5.

Pore connectivity, a critical parameter for thermal and fission products transport, increases markedly toward the periphery. Fig. 5 demonstrates that both the average pore volume and inter-pore proximity decrease sharply near the FCCI region. This clustering facilitates the percolation of fission gases and promotes the formation of interconnected pore networks [24,25]. Notably, the FCCI region exhibits the most densely packed pore distribution across the entire cross-section.

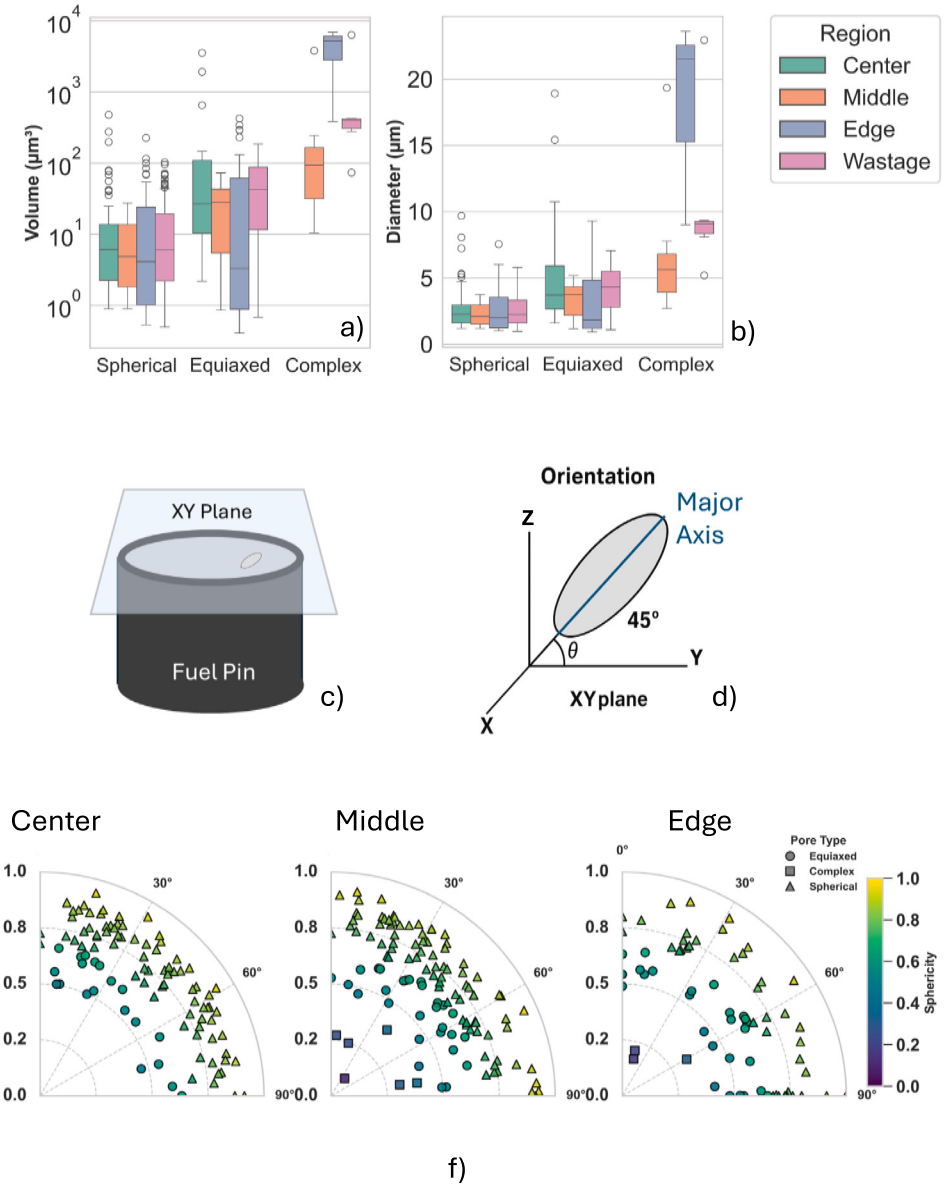

Fig. 4. Representative segmentation and analysis of pore structures across distinct fuel regions. (a–b) Pore size distribution by morphological classification; (c–f) orientation of pores with respect to equivalent diameter.

Even at similar porosity fractions, the proximity of pores enables contiguous pathways for fission product migration and phase boundary infiltration. Previous studies using neutron tomography and SEM–EDS analysis suggest that this clustering is associated with early lanthanide deposition at the cladding interface [4,23].

The closeness of the pore network here aligns with mechanistic FCCI models, which posit that pore-facilitated lanthanide mobility is a primary driver for pellet cladding chemical interaction [4,29]. It also reinforces that traditional porosity volume fraction alone is insufficient—spatial metrics such as connectivity and tortuosity must be considered to accurately model fuel degradation mechanisms. Additionally, an internal pore permeability analysis was conducted using a simulated percolation test applied at the sample edges [31]. This approach was used to estimate the mobility of fission gases and products within the fuel, as these species are known to diffuse and migrate through the interconnected pore network.

The percolation test was implemented using a three-dimensional flood-fill simulation. Starting from all six external faces of the volume, voxels belonging to the pore phase were iteratively labeled as "flooded" if they were connected by 26 nearest-neighbor voxels that had already been flooded. A 26-voxel neighborhood was chosen because it captures all face-, edge-, and corner-touching connections, which are physically meaningful in voxelized tomography data. More restrictive definitions (e.g., 6- or 18-connectivity) artificially break diagonal or tortuous pore pathways due to digitization effects, leading to an underestimation of long-range connectivity. Using the full 26-neighbor criterion, therefore, ensures a realistic reconstruction of pore continuity and avoids spurious fragmentation within the percolating network. This iterative dilation procedure continued until no further pore voxels could be reached from the boundary. The fraction of the total pore volume that became flooded defined the permeability percentage, which represents the portion of pores participating in long-range transport pathways.

The percolation threshold was identified as the minimum connectivity radius at which a spanning cluster forms across the domain. In practice, this corresponds to the condition in which the flood-fill pore propagates continuously from one face of the sample to the opposite face. Operationally, we defined the threshold as the lowest connectivity distance r_c for which more than 50% of the pore volume

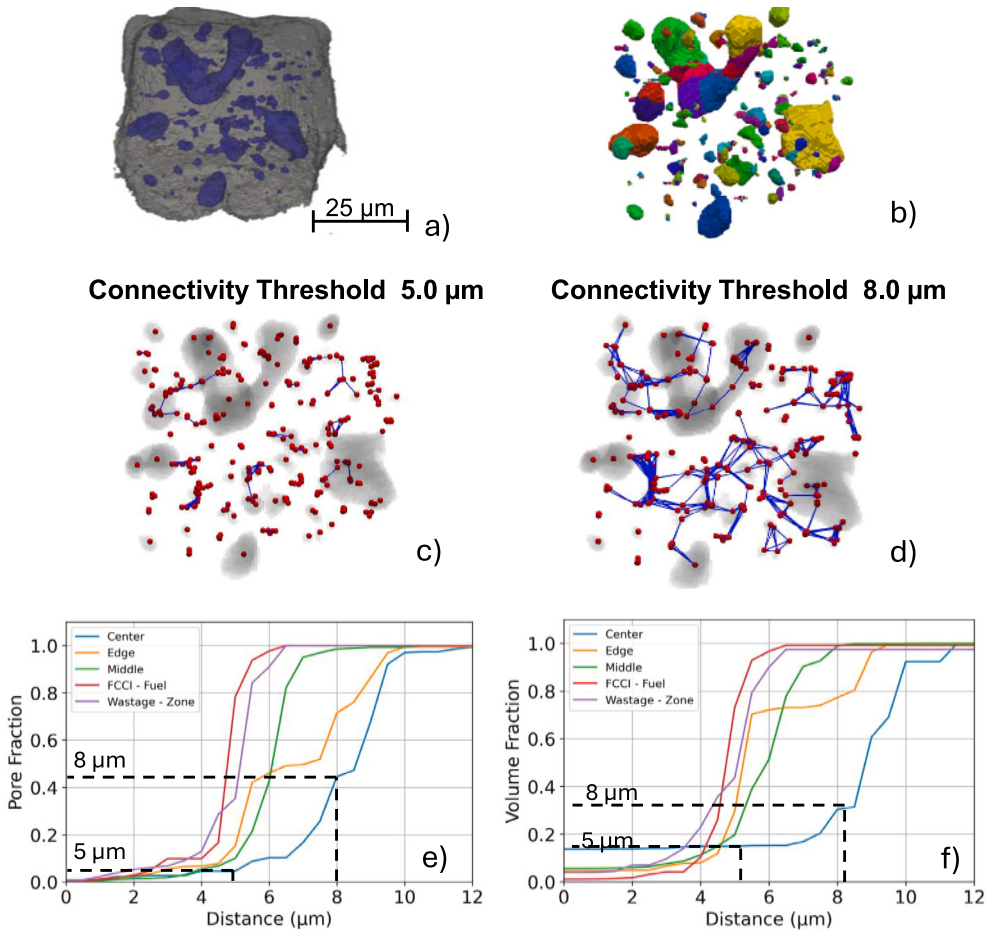

Fig. 5. (a) Reconstructed tomographic volume with segmented pores (blue). (b) Individual pores separated using watershed segmentation, enabling centroid-based connectivity analysis. (c–d) Pore network graphs overlaid for connectivity thresholds of 5.0 µm and 8.0 µm, respectively; red nodes represent pore centroids and blue lines denote pairwise connections. (e, top right) Cumulative pore count fraction as a function of distance threshold. A steep rise in the curve indicates that pores in a given region are closely spaced and rapidly form a connected network (e.g., FCCI-fuel and wastage zones), whereas gradual increases (e.g., center) indicate more dispersed pores. (f, bottom right) Cumulative volume fraction vs distance threshold. This curve shows the fraction of total pore volume that becomes connected at increasing distances, highlighting the influence of large interconnected pores in specific regions like the FCCI-fuel interface.

belonged to this spanning cluster, consistent with standard percolation models [31]. This criterion provided a reproducible estimate of the onset of long-range permeability within the pore network.

Fig. 6 presents a permeability analysis conducted on different regions of the fuel. Fig. 6a shows the center of the fuel, where the segmented pore structure, raw tomographic slice, and rendered 3D pore network reveal mostly isolated pores, resulting in a calculated permeability of 36%. In Fig. 6b, corresponding to the middle of the fuel, a more interconnected and complex pore network is observed, leading to a significantly higher permeability of 87%. Fig. 6 illustrates the edge of the fuel. Here, the pores are highly connected and form large, continuous pathways, resulting in the highest permeability measured at 93%. Finally, Fig. 6d focuses on the fuel-cladding interface (FCI), showing the interface between U–10Zr and HT9 steel. Although some degree of pore continuity is present, this region exhibits a reduced permeability of 52%, likely influenced by interfacial densification and the formation of secondary intermetallic phases that introduce constrictions, dead-end pathways, and increased tortuosity near the fuel-cladding interface. In addition, the finest pore throats in the FCCI region approach the spatial resolution limit of the tomography, which may further reduce the number of resolved long-range transport pathways. Despite this reduced permeability, lanthanides exhibit rapid migration toward the fuel surface, forming distinct La-rich phases near the cladding even at low burnup levels. This behavior is consistent with short-range connectivity and vapor- or surface-assisted transport through densely clustered, interconnected pores, which can efficiently deliver lanthanides to the interface without requiring fully percolating, system-spanning pore networks.

Before Na ingress, lanthanide transport is the superposition of slow lattice diffusion and faster *surface* diffusion along internal pore walls. In low-connectivity regions (center), surface segments are isolated and do not form long-range routes; in high-connectivity regions (middle/edge and FCCI-adjacent), the internal surface behaves as a continuous 3D pathway, qualitatively increasing the effective Ln diffusivity at comparable porosity. Once the connected network vents and admits Na, the pore phase becomes a high-diffusivity channel that is bicontinuous, such that even moderately connected porosity can disproportionately accelerate migration of Ln to the cladding, thereby increasing FCCI kinetics [30]. Furthermore, atomistic simulations reveal strong segregation of Ce and other lanthanides to the interface, driven by their low surface energies and enhanced thermodynamic preference for the fuel periphery [29].

Localized porosity evolution

To explore the relationship between pore morphology and local chemistry, each pore was classified based on the dominant surrounding phase using grayscale contrast from tomographic 3D data in Fig. 7. Zr-rich phases appeared dark and U-rich phases are bright, enabling a three-phase classification: Zr-rich, U-rich, and (U, Zr)- rich or mixed compositional distribution. This visual method is consistent with trends

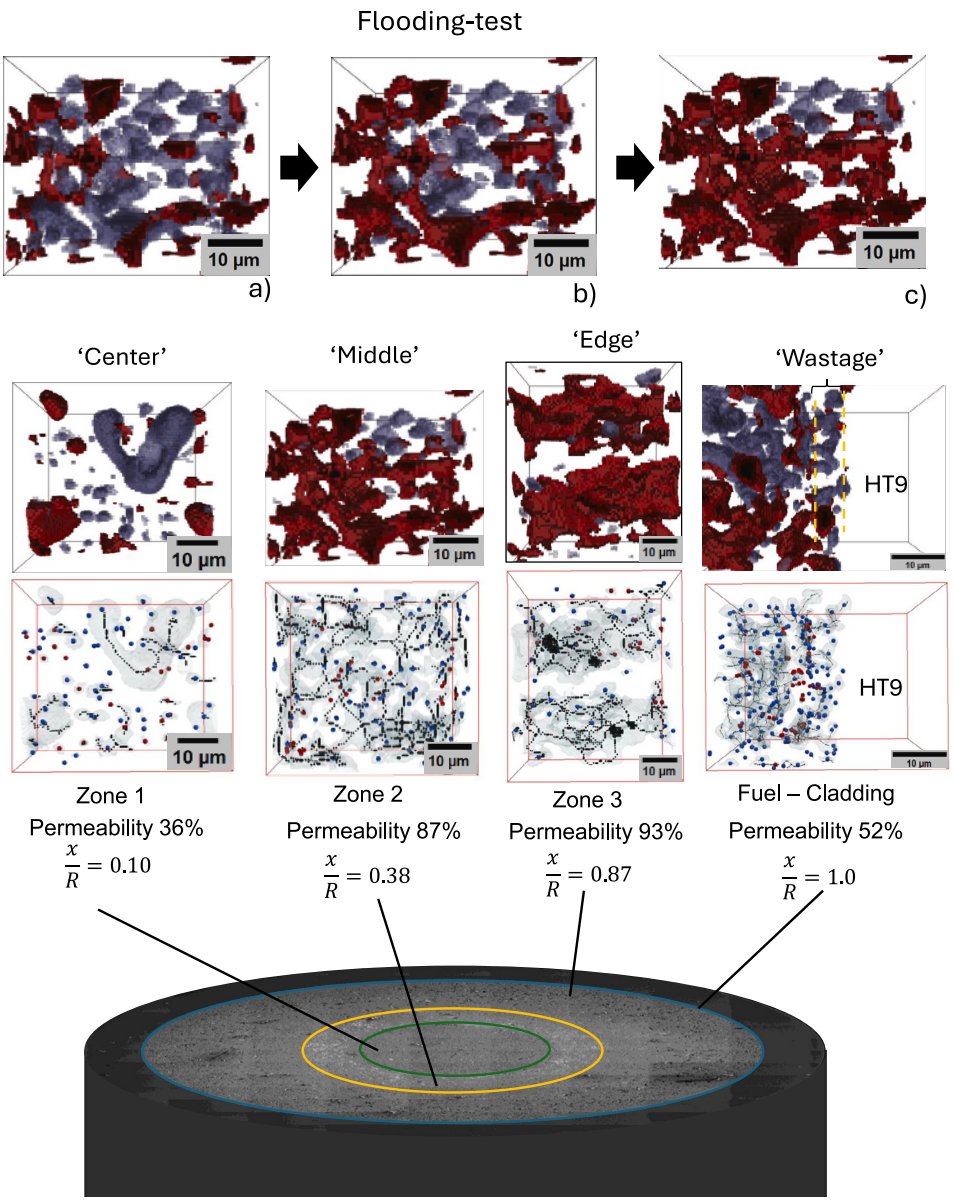

Fig. 6. Permeability test across different fuel regions based on 3D tomographic analysis to determine the interconnectivity of the pores.

identified in high-resolution TEM–EDS studies and was validated across multiple tomographic slices to reduce segmentation artifacts and ensure 3D spatial coherence. It is noted that the identification of Zr-rich and U-rich regions in the XCT datasets is based on relative grayscale contrast and is therefore correlative rather than quantitatively compositional. Grayscale variations in phase-contrast XCT arise from a combination of local density differences, phase composition, and imaging conditions, and were not calibrated to absolute elemental concentrations in the present study. The grayscale-based classification is supported by prior site-matched SEM/EDS and XRF-CT analyses reported in the literature for irradiated U–Zr fuels, which show consistent spatial partitioning of Zr-rich and U-rich phases. Accordingly, the grayscale contrast is used here to distinguish relative phase regions and trends in porosity evolution, rather than to infer precise local chemistry.

A clear radial progression emerged that reflects the three-zone Zr redistribution model reported by both Salvato et al. and Xu et al. [3,22]. In Zone 1 (fuel center, $R < 0.32$), pores were embedded predominantly in the Zr-rich or mixed regions, consistent with the γ_2 matrix and δ-UZr_2 precipitates observed in TEM analyses [32]. These surroundings promote the formation of small spherical pores, and Xu et al. independently reported that Zone 1 (Center) exhibited the lowest porosity overall, dominated by small, well-contained pores. Mechanistically, this tendency can be rationalized by the stability of Zr-rich phases: δ-UZr_2 is the only intermetallic in the U–Zr system, stable across a broad Zr-rich composition range, and forms a coherent scaffold that constrains pore growth [33,34]. The high interfacial energy and limited diffusivity in these matrices impose an energetic penalty on pore elongation, thereby favoring spherical morphologies and suppressing coalescence.

In Zone 2 (Middle) ($0.32 < R < 0.48$), pores increasingly appeared within U-rich environments, dominated by α-U and distorted α/β-U phases. Xu et al. identified this as the most Zr-depleted region, characterized by oxidation-prone surfaces and intermediate pore sizes. This zone also showed the highest proportion of equiaxed and complex pores in our analysis, along with more varied pore orientations, suggesting active coalescence and reduced constraint by the surrounding matrix. These observations are consistent with Salvato et al.'s report of surface degradation and amorphous transformation zones in this region.

By Zone 3 (Edge) ($R > 0.48$), the phase environment shifted back toward Zr-rich domains, including γ_2 and finely dispersed δ-UZr_2

phases. Xu et al. quantified this outer region (especially Zone 3) as having the highest porosity contributions from large and irregularly shaped pores (tortuous), exceeding 5% of the total pore volume. Our tomography corroborates this, showing a strong return to Zr-rich phase surroundings (Fig. 3) and a predominance of complex morphologies with high inter-connectivity.

Fig. 7 summarizes the spatial evolution of pore environments and surrounding phase chemistry across the fuel radius. Panel (a) shows representative grayscale tomographic cross-sections extracted from the center, middle, and edge of the fuel, revealing clear differences in matrix contrast and pore morphology. Panel (b) provides the corresponding chemical-contrast maps, highlighting regions enriched in UZr_2 (Zr-rich) and α-U (U-rich), and illustrating the outward increase in Zr-rich domains. Panel (c) quantifies the dominant phase surrounding each pore, showing that pores transition from U-rich environments at the center to predominantly Zr-rich surroundings at the edge. Finally, panel (d) presents violin plots of the UZr_2-rich / (UZr_2-rich + α-U-rich) ratio, demonstrating a progressive chemical shift toward Zr-rich matrices with increasing radial position. Together, these four panels establish the strong coupling between local chemistry and pore evolution, providing the chemical framework required to interpret the radial trends in morphology and connectivity observed in U–10Zr.

These findings highlight a strong coupling between local chemistry and pore evolution. Zr-rich matrices (Zones 1 and 3) tend to constrain pore shape and limit coalescence through phase stability and interfacial energy effects, whereas the U-rich zones (Zone 2) promote anisotropic growth, increased connectivity, and morphological complexity. The role of Zr as a stabilizer in U–Zr alloys has been demonstrated in both thermodynamic assessments [34,35] and microstructural studies of Zr-rich alloys [33], as well as in its ability to stabilize secondary phases and reduce fission product mobility [36]. These trends, emerging independently from tomography, deep-learning-based SEM analysis [22], and high-resolution TEM–EDS characterization [3], underscore the robustness of this phase-morphology framework in high burnup U-10Zr fuels.

Fuel cladding chemical interaction

FCCI is one of the main degradation mechanisms in metallic fuel systems, especially as burnup and temperature increase. The 3D rendering shown in Fig. 8 highlights the complex structure of the fuel-cladding interface. The 2D cross-sectional views reveal the formation of Fe-rich intermetallics and a narrow wastage zone, while the enhanced contrast 3D rendering makes it clear that Fe diffusion into the fuel is spatially non-uniform. The irregular interface front suggests directional diffusion likely guided by sinks such as grain boundaries, pores, or other microstructural pathways—features difficult to capture in 2D alone. This volumetric context is especially important for understanding how FCCI may evolve asymmetrically around the fuel perimeter. The depth-resolved slices highlight the unique distribution of Fe-intermetallics in the fuel zone. Fig. 8b shows the logging of metallic into isolated pore sites, while in Fig. 8c–d, there is a reaction of HT-9 cladding and intermetallics with the fuel front, which leads to a dominant reaction front in the fuel zone.

Fig. 9 provides a higher-resolution look at elemental distributions across the same region using energy-dispersive X-ray spectroscopy (EDS). Elemental maps show strong segregation of Fe and Cr in the cladding, with U and Zr localized on the fuel side. The interfacial zone—marked by Fe diffusion and Zr depletion—suggests limited interdiffusion, with a relatively clean transition band. Ce, although detected, appears localized to the fuel side without significant migration into the cladding. This observation is consistent with early-stage FCCI under moderate temperatures and burnup conditions [37]. Notably, the absence of a broad Ce diffusion front supports previous in-pile observations by [4], who showed that lanthanide-driven FCCI becomes more prominent at higher temperatures and in hotter axial regions of the fuel pin.

One of the more relevant aspects in modeling and understanding FCCI is capturing the mechanistic basis of lanthanide and intermetallic diffusion. Atomistic simulations using the Bozzolo–Ferrante–Smith (BFS) method [29] have shown that Ce and other lanthanides exhibit strong surface segregation due to their extremely low surface energies. These simulations demonstrate that Ce has the highest surface affinity, followed by Pr, and that annealing promotes the formation of Ce–Zr solid solutions and lanthanide-rich precipitates. These behaviors align well with experimental observations of FCCI initiation and help explain why even small Ce enrichment near the interface can signal the beginning of the reaction. Although the Ce distribution observed in Fig. 9 is relatively limited, and is found prominently in the wastage zone, its presence still indicates the potential for future lanthanide-driven degradation.

From a transport and materials perspective, even narrow FCCI layers – particularly those enriched in Fe intermetallics – can significantly affect chemical diffusivity and local thermal conductivity. More critically, the interfacial region observed here shows signs of porosity or cracking within the wastage zone, as seen in Fig. 8. This suggests the reaction zone is not entirely stable but instead may be structurally compromised. Such features are consistent with embrittlement caused by the formation of brittle Fe-based intermetallic phases, which are known to degrade mechanical integrity. Rather than acting solely as diffusion barriers, these zones may also serve as initiation sites for mechanical failure under thermal cycling or stress. This is consistent with prior FCCI studies that linked void formation and cracking to the growth of intermetallics in irradiated U-Zr systems. Additionally, as noted by [38], the presence or absence of a continuous Zr-rich layer can further influence how rapidly and severely this degradation occurs. It is also important to recognize that our analysis is limited to a 50 μm liftout volume due to radiological constraints. While this provides valuable resolution, it may miss larger-scale or asymmetric FCCI features developing elsewhere in the pin. Still, the integration of 3D imaging, elemental mapping, and compositional profiling in this dataset provides strong evidence for localized FCCI complex diffusion paths.

A closer inspection of the 3D reconstructions and segmented Fe profiles (Figs. 8, 10) reveals that the diffusion front is not planar but exhibits a waviness consistent with anisotropic advancement. Such asymmetric advancement of the interfacial reaction front is consistent with circumferential variations in cladding temperature; hotter azimuthal sectors are known to accelerate Fe diffusion and intermetallic formation [4,14]. Regions of enhanced penetration coincide with pore-rich or boundary-dense domains, while adjacent dense zones remain relatively unreacted. Similar asymmetric front morphologies were reported in FFTF MFF-3 and MFF-5 pins, where Capriotti et al. identified thicker wastage zones on the thermally hotter sides of the cladding, reflecting a strong radial and circumferential bias in FCCI progression [39]. This directional dependence indicates that the local microstructure acts as a set of “fast lanes” and “slow lanes” for interdiffusion.

The elemental maps in Fig. 9 further support this interpretation. Ce enrichment is restricted to the fuel side, localized near pore structures, consistent with previous reports that lanthanides migrate rapidly along thermal gradients and preferentially precipitate in connected porosity at the periphery [40]. The contrast with helium-bonded annular U-10Zr fuels, where negligible lanthanide penetration into the cladding was observed [37], underscores the critical role of sodium-infiltrated porosity in enabling directional transport. In sodium-bonded fuels, interconnected pores act as high-diffusivity radial highways delivering lanthanides directly to the cladding, whereas in sodium-free designs, this pathway is suppressed and FCCI is correspondingly muted.

Finally, the statistical spread in Fe penetration depths quantified in Fig. 10 demonstrates that local transport is highly heterogeneous, with some regions exhibiting nearly twice the mean diffusion length.

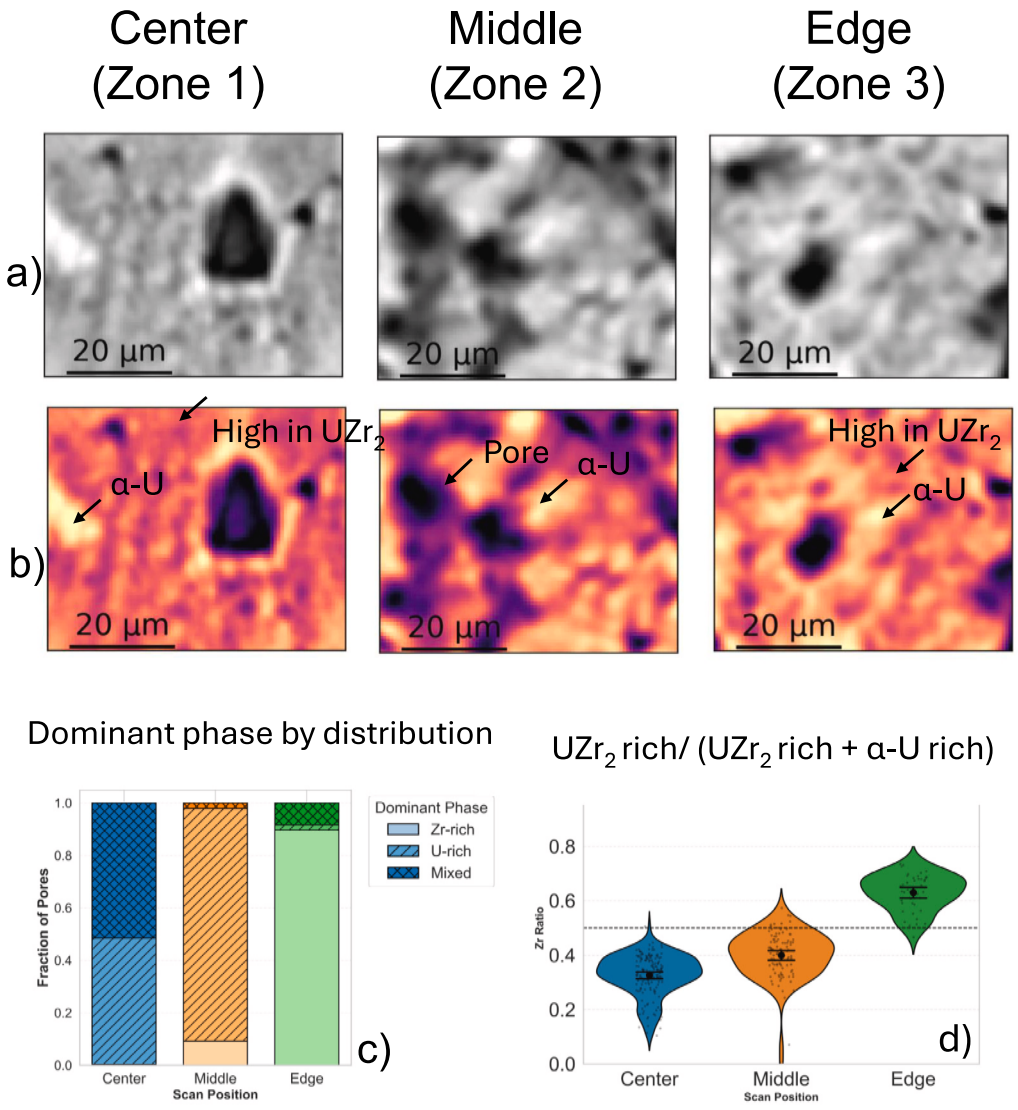

Fig. 7. Radial evolution of U–Zr phase and pore environments revealed by tomographic cross-sections. Panel (a) shows grayscale tomographic slices from the center, middle, and edge, revealing increasing microstructural heterogeneity with radius. Panel (b) maps UZr_2 (Zr-rich) and α-U (U-rich) regions, highlighting a clear shift from U-rich surroundings at the center to Zr-rich domains toward the edge. Panel (c) quantifies the dominant phase around each pore, confirming this transition, while panel (d) shows the corresponding UZr_2-rich / (UZr_2-rich + α-U-rich) ratio. Overall, these results demonstrate that pore evolution occurs within distinct local chemical environments that evolve systematically across the fuel radius.

The distribution of Fe diffusion distances is strongly skewed, with the mean value exceeding the median, indicating highly heterogeneous transport behavior at the fuel-cladding interface. This heterogeneity arises because Fe penetration is not uniform but instead localized along preferential microstructural pathways associated with connected pore clusters, phase boundaries, and regions undergoing intermetallic formation. While most interface regions exhibit relatively limited Fe penetration, a small number of locally enhanced transport paths enable significantly deeper diffusion, producing a long-tailed distribution and elevating the mean relative to the median. This variability aligns with recent mechanistic multiscale modeling work, which shows that lanthanide transport is governed by a combination of slow lattice diffusion, faster surface diffusion along pores, and extremely rapid sodium-assisted transport through interconnected networks [30]. The effective diffusivity controlling FCCI is therefore anisotropic and connectivity-dependent, scaling with the degree of pore interconnection and alignment with the radial thermal gradient. Our experimental observations are therefore consistent with predictive phase-field models that treat FCCI as a directionally biased phenomenon rather than a uniform interdiffusion process [41].

The observations above indicate that FCCI onsets where Ln supply to the interface becomes transport-controlled rather than reaction-controlled. In U–Zr, Ln mobility is strongly enhanced along internal surfaces and through any sodium-logged porosity; thus, how porosity is connected in the near-edge microstructure governs the apparent Ln diffusivity feeding the reaction front. In sodium-bonded or Na-logged conditions, the interconnected pore skeleton acts as a high-diffusivity pathway that can outpace solid-state diffusion, accelerating Ln delivery to the cladding and promoting Fe–Zr intermetallic formation [e.g. 29, 37]. This explains why our EDS/3D results show early Ln presence on the fuel side of the interface without a broad penetration into HT9 (Fig. 9): the rate-limiting step is Ln transport to the interface within the fuel, not diffusion into the cladding.

The measured interface roughness (Fig. 8) and the radial bias in pore orientation/morphology (Fig. 4) are consistent with a diffusion field that is anisotropic: (i) a strong radial thermal gradient ($\partial T/\partial r > 0$) and stress field drive Ln flux outward, (ii) short inter-pore distances and tortuous connectivity near the edge provide preferential radial pathways, and (iii) circumferential heterogeneities (grain-boundary density,

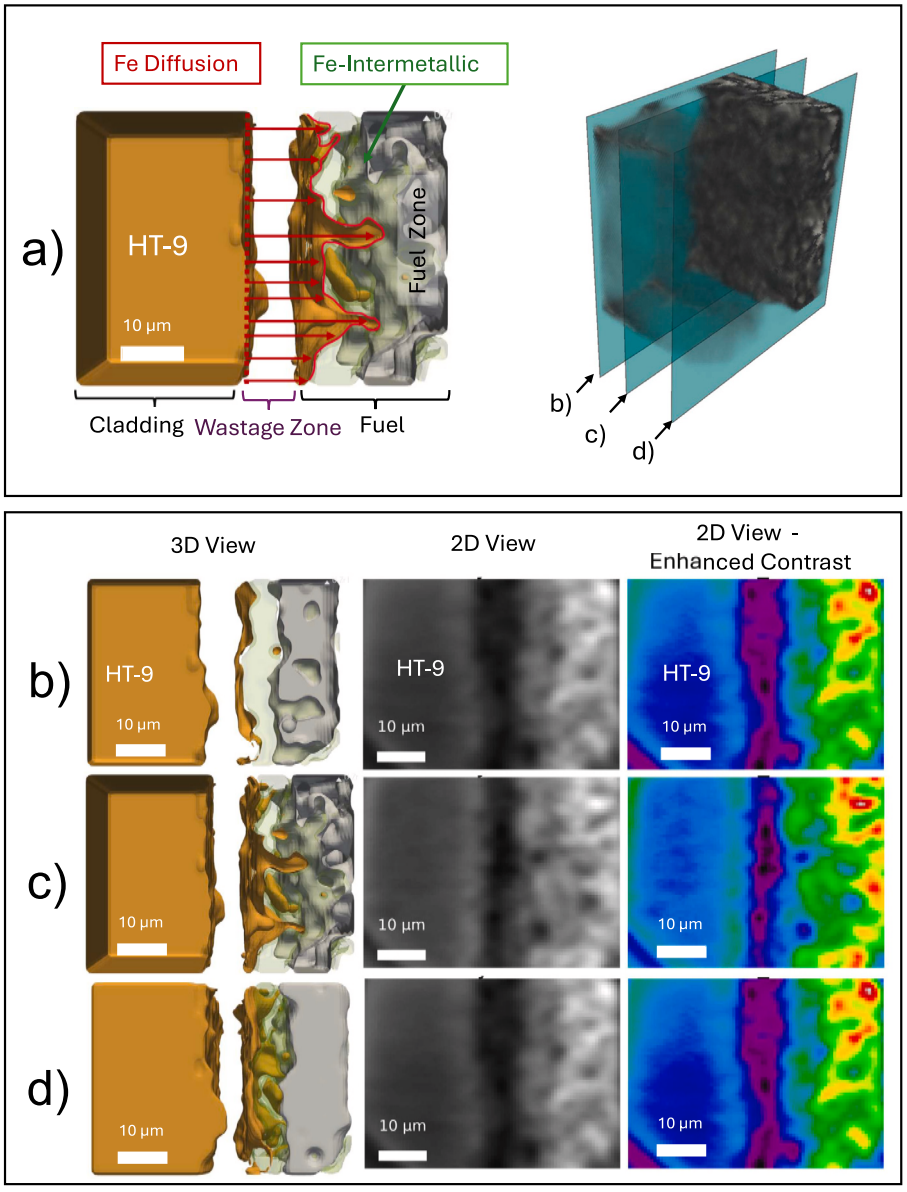

Fig. 8. Analysis of iron diffusion across the fuel-cladding interface. **(a)** 3D rendering from X-ray micro-CT showing the view of the interface region, and depth-resolved slices showing the heterogeneity in the FCCI zone. **(b–d)** Segmented zones of depth-resolved slices identifying the Fe-rich cladding (HT-9), interfacial Fe-intermetallic phase, and fuel region. The analysis quantifies the spatial distribution and penetration depth of Fe as a function of diffusion distance (µm).

local porosity, and Fe intermetallic patches) produce the observed azimuthal waviness of the reaction front. In this picture, the interface advances faster along microstructural "fast lanes" (connected porosity aligned toward the radius, high boundary density) and advances more slowly across denser, Zr-rich, or recrystallized pockets—consistent with the asymmetric Fe penetration depths and the narrow wastage layer we quantify (Figs. 8, 10) [4,5].

These results support an FCCI mechanism in which (a) the radial component of the Ln/Na flux dominates the early growth at the periphery, (b) local interconnection and tortuosity—rather than porosity fraction alone—control the supply rate, and (c) the cladding response remains limited to a thin interdiffusion/intermetallic band until sustained Ln supply is established. Accordingly, predictive models should include a connectivity-aware effective diffusivity in the fuel (sensitive to porosity interconnection and possible Na logging) coupled to temperature/stress fields to capture the observed directional advance of the reaction front [4,29,37].

Effective thermal conductivity models

To capture the impact of porosity and sodium logging on heat transport, several effective thermal conductivity models are employed. The pore-phase conductivity is defined as a mixture of fission gas (void) and sodium contributions, scaled by the fraction of porosity filled with sodium f_{Na}:

$$k_{pore}(f_{Na}, T) = (1 - f_{Na})\, k_{air}(T) + f_{Na}\, k_{Na}(T),$$

where $k_{air}(T)$ and $k_{Na}(T)$ are temperature-dependent correlations for gas- and sodium-filled pores, respectively. This formulation interpolates between the limiting cases of fully air-filled and fully sodium-filled porosity.

The Maxwell–Eucken formulation provides a classical baseline for isolated pore behavior, while the Karahan-type correction incorporates metallic-fuel-specific effects including Zr content, temperature dependence, porosity, and sodium logging. Together, these models bracket physically meaningful limits of heat transport in U–10Zr fuel and

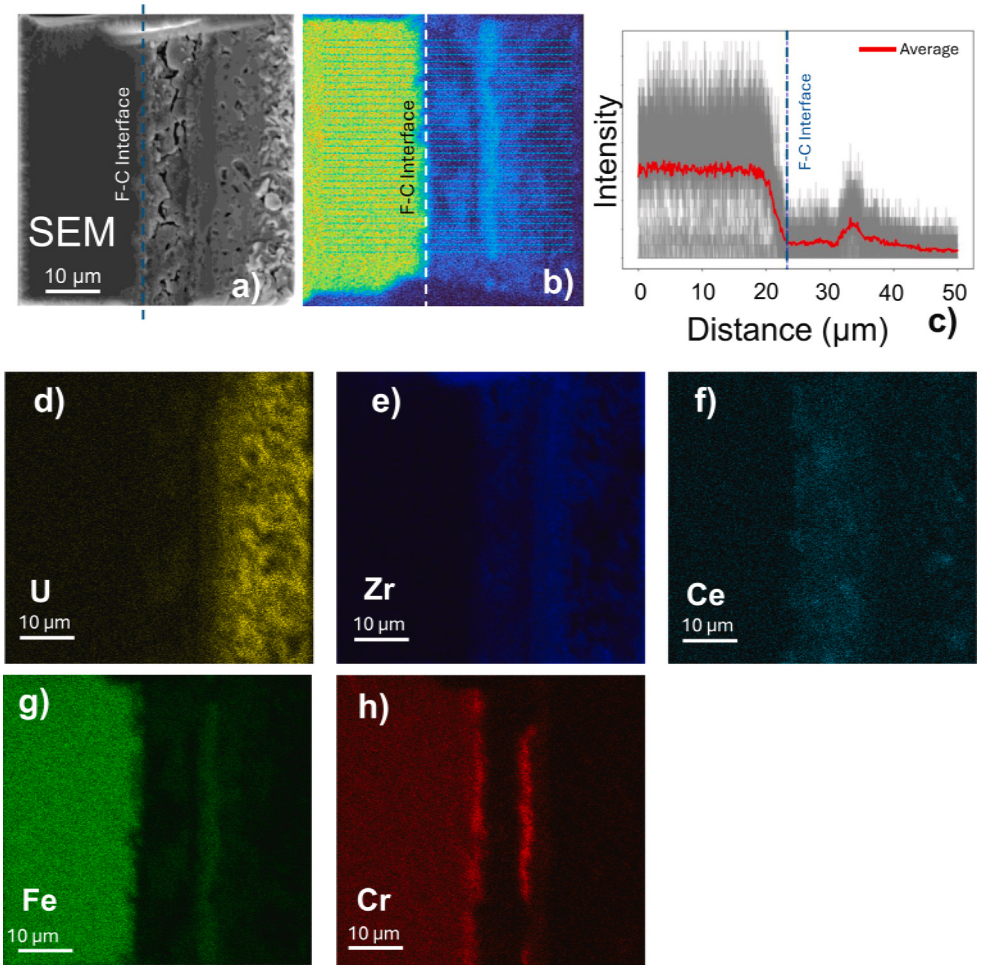

Fig. 9. (a) Scanning electron microscopy (SEM) image highlighting the interface, (b) 2D chromium–iron (Cr–Fe) distribution, (c) averaging of the elemental Cr–Fe line scan, and the corresponding energy-dispersive X-ray spectroscopy (EDS) of the elemental maps for (d) uranium (U), (e) zirconium (Zr), (f) cerium (Ce) (g) iron (Fe) and (h) chromium (Cr) distributions. Each EDS map highlights the spatial distribution of individual elements across the fuel-cladding interface.

enable direct interrogation of how pore morphology and connectivity—resolved experimentally via 3D tomography—impact local thermal performance. More comprehensive fuel performance simulations, such as those implemented in finite-element codes (e.g., BISON), explicitly solve coupled thermo-mechanical and irradiation effects at the pin scale. While such approaches are essential for integral reactor analyses, they represent a distinct modeling framework and are beyond the scope of the present microstructure-resolved study.

At low to moderate porosity, the Maxwell–Eucken relation treats pores as spherical inclusions in a continuous solid matrix and predicts a smooth decrease in k_{eff} with porosity ϕ [42]. At higher porosities, transport is limited by the connectivity of the solid skeleton. To represent this regime, a percolation-type model captures the sharp drop in thermal conductivity once ϕ exceeds the critical threshold $\phi_c \approx 0.8$ for random 3D networks. To represent the dense fuel matrix itself, a Karahan-style corrected conductivity is employed [43]:

$$k_f(\phi, T) = k_0(T)\, F_{\mathrm{Zr}}(W_{\mathrm{Zr}})\, P_c(\phi, f_{\mathrm{Na}}),$$

where $k_0(T)$ is the base U–Zr conductivity, F_{Zr} accounts for Zr content, and P_c introduces a porosity/logging correction. In line with prior analyses, sodium logging is typically assumed to become significant once $\phi \gtrsim 0.25$.

Figs. 11 and 12 illustrate the influence of pore morphology, sodium infiltration, and radial position on k_{eff}. As porosity ϕ increases, k_{eff} decreases, reducing the overall heat flux. Furthermore, isolated spherical pores lead to a gradual decrease in the thermal conductivity, while interconnected pores accelerate degradation due to reduced solid connectivity. Sodium infiltration partially offsets this degradation: sodium-logged interconnected pores retain higher k_{eff}, especially at elevated temperatures where the $k_{\mathrm{Na}}/k_{\mathrm{solid}}$ ratio is large (Fig. 11). Radial analysis (Fig. 12) shows that sodium logging has the strongest mitigating effect in the middle and edge regions, though the overall trend remains governed by the intrinsic decrease of the U–Zr matrix conductivity with temperature.

These results demonstrate that both pore morphology (isolated versus interconnected) and sodium logging govern the effective thermal conductivity of U–10Zr fuel. Nonlinear effects become increasingly significant as pore density and connectivity increase, underscoring the need for connectivity-aware models in fuel performance modeling.

Implications for fuel performance

The three-dimensional pore analyses presented here provide critical insights into how microstructural heterogeneity governs the macroscopic performance of irradiated U–10Zr fuel. In particular, porosity orientation, connectivity, and phase-specific surroundings collectively define pathways for fission gas release, lanthanide migration, and sodium infiltration. These attributes cannot be captured by porosity fraction alone, underscoring the importance of connectivity-aware metrics for predictive modeling.

Pore orientation has a strong impact on mass transport processes. The transition from randomly oriented spherical pores in the fuel

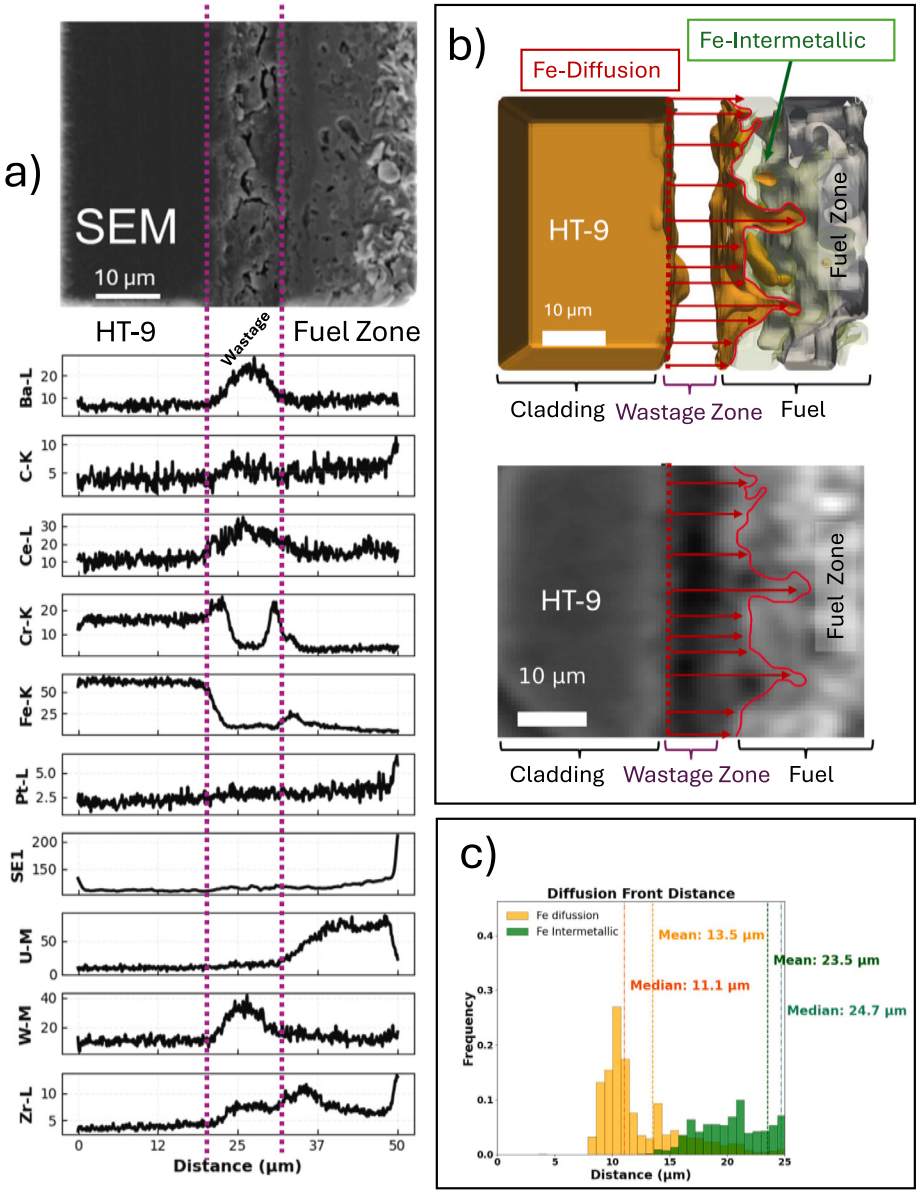

Fig. 10. **(a)** EDS compositional line profiles showing elemental intensities across the fuel-cladding interface, highlighting Fe diffusion and intermetallic formation. **(b)** 3D reconstruction of the XCT data of the fuel-cladding region illustrating interfacial morphology and microstructural transitions. **(c)** Distribution of Fe diffusion distances extracted from segmented profiles, quantifying the extent of Fe migration from the HT-9 cladding into the fuel region.

center to radially aligned equiaxed and complex pores near the edge (Zones 2–3, Fig. 1) produces preferential channels that align with the temperature gradient. These radially oriented networks effectively act as "highways", enabling rapid outward migration of fission gases and lanthanides. The alignment also increases the likelihood of pore–pore coalescence, accelerating the formation of contiguous, percolating clusters. Such anisotropic networks explain the observed waviness of the FCCI front (Fig. 8), where reaction zones advance faster along porous domains than across denser, Zr-rich pockets [3,39].

The combined effects of pore connectivity and sodium infiltration strongly affect heat transport. Effective thermal conductivity models (Figs. 11, 12) demonstrate that isolated pores primarily act as free volume, producing a smooth conductivity degradation consistent with Maxwell–Eucken scaling. In contrast, sodium-logged interconnected pores retain significant transport capability, partially mitigating the conductivity drop predicted for high-porosity regions. This effect is most pronounced in the edge and FCCI zones, where pore networks are both dense and radially aligned. The Karahan-style correction highlights that the balance between Zr content, porosity fraction, and sodium logging determines the local k_{eff}, with sodium infiltration mitigating up to 30%–40% of the conductivity loss at elevated temperatures [43].

Furthermore, pore topology has a direct impact on FCCI kinetics. The high pore density measured near the fuel-cladding interface, which is estimated to be 6.0×10^{6} pores/mm^{3}, results in short transport lengths and surface area for lanthanide migration. Our permeability tests confirm that the FCCI-adjacent region maintains a highly interconnected network, even at moderate porosity volume fractions. This connectivity accelerates Ce and other lanthanide transport to the interface, supplying reactants to drive Fe–Zr intermetallic growth [29,30]. In this regime, the onset of FCCI becomes transport-controlled rather than reaction-controlled, governed by the availability of connected pathways within the fuel rather than by bulk diffusion through the cladding.

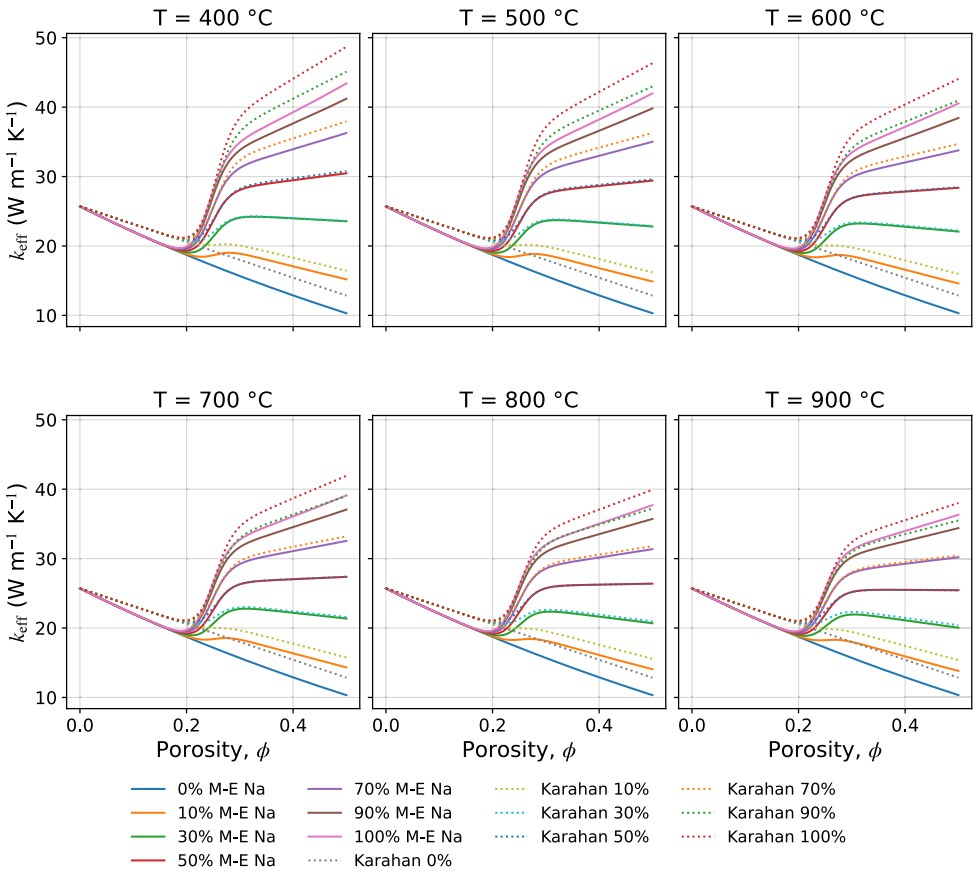

Fig. 11. Effective thermal conductivity k_{eff} of U–10 wt% Zr fuel as a function of porosity ϕ at selected temperatures (400–900 °C). Solid curves correspond to the Maxwell–Eucken model, while dotted curves denote the Karahan correction method that explicitly accounts for the combined effects of Zr content and pore saturation by sodium. Multiple sodium fill fractions (f_{Na} = 0–100%) are shown for each case. Sodium infiltration mitigates the conductivity loss relative to dry (air-filled) pores, and the Karahan method predicts systematically higher k_{eff} values than Maxwell–Eucken, especially at elevated temperatures where the k_{Na}/k_{solid} ratio is large.

Overall, radial variations in the temperature gradient, irradiation, and stress field promote constituents redistribution, eutectic and intermetallic formation, resulting in spatially heterogeneous Zr/U ratios that govern local pore evolution. In regions with pronounced compositional partitioning, pores evolve from isolated, equiaxed to elongated morphologies with a preferred orientation along the radial direction, thereby increasing connectivity and permeability. This interconnected pore network enables efficient transport of fission products and sodium logging at high temperatures, thereby increasing the effective contact area at the fuel-cladding interface and accelerating FCCI kinetics. Hence, the coupled evolution of local phase composition and pore morphology provides a direct mechanistic pathway linking thermo-mechanical conditions to FCCI progression.

While the present analysis is based on site-specific, microstructure-resolved volumes, the observed pore topology trends provide insight into local transport mechanisms that underpin macroscopic fuel behavior. The highly connected pore networks identified in this study should be interpreted as localized microstructural states that arise under specific thermal, compositional, and irradiation conditions along the fuel radius, rather than as uniformly pervasive features throughout the fuel rod. As such, direct one-to-one extrapolation to full rod-scale behavior is not implied. Instead, the quantitative pore morphology, connectivity, and permeability metrics reported here provide physically grounded inputs and constraints for multiscale or homogenized fuel performance models, informing how local microstructural states influence effective thermal transport and FCCI progression at larger scales.

Finally, these findings carry broader implications for fuel design and performance modeling. Since porosity fraction alone cannot predict transport or degradation, future models must incorporate spatial metrics such as connectivity, tortuosity, and pore orientation. Moreover, sodium bonding conditions play a decisive role: in Na-bonded fuels, infiltrated porosity creates high-diffusivity radial highways for fission products, while in sodium-free configurations this pathway is suppressed. Together, these results demonstrate that site-specific microstructural features strongly dictate heat and mass transport, cladding interaction, and mechanical integrity in U–10Zr metallic fuels.

Conclusions

This study provides the first site-specific three-dimensional analysis of porosity evolution and connectivity across all four radial regions of neutron-irradiated U–10Zr fuel. The key findings are:

I. Quantitative 3D analysis reveals a clear radial gradient in porosity, increasing from 5.5% at the center to over 10.5% near the edge, consistent with swelling behavior driven by fission gas pressure and matrix compliance.
II. Pore density exhibits a sharper increase than porosity volume, rising by nearly two orders of magnitude in FCCI regions (up to 6.0×10^6 pores/mm^3). This indicates the onset of highly fragmented and spatially dense pore populations at the fuel-cladding interface.
III. Morphological and orientation analyses show a progression from spherical pores in Zr-rich central zones to equiaxed and complex pores near the periphery, with increasing radial alignment. This anisotropy promotes outward fission gas migration and provides preferential diffusion pathways for lanthanides.

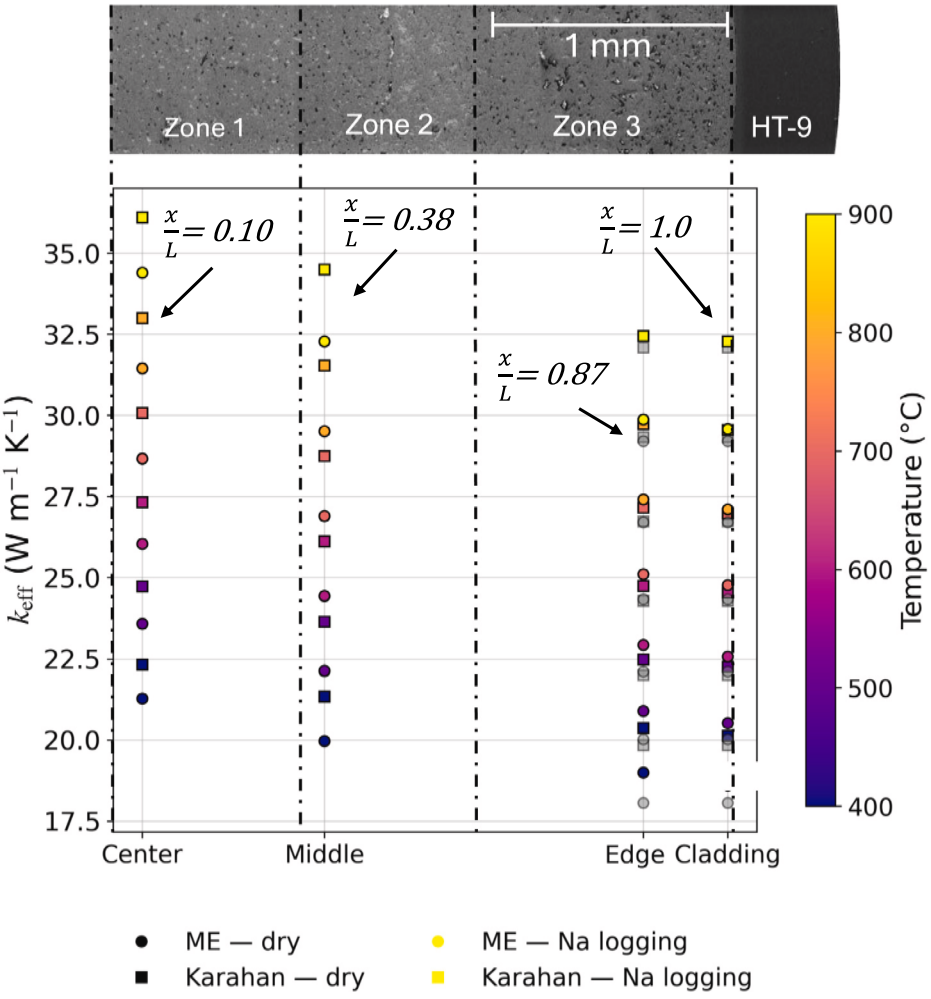

Fig. 12. Effective thermal conductivity k_{eff} of U–10 wt% Zr fuel as a function of radial position (x/L) from the centerline to the fuel-cladding interface (HT-9). Four characteristic regions are shown based on correlation with the scanning electron microscope image: Zone 1 (center), Zone 2 (middle), Zone 3 (edge), and Zone 4 (cladding interface). Results are obtained from both Maxwell–Eucken (circles) and Karahan (squares) models. Colored dotted curves denote sodium-logged porosity, with the color scale indicating temperature (400–900 °C). For comparison, dashed curves show the dry (no-logging) case. Sodium infiltration mitigates conductivity loss, particularly in the middle and edge zones, though the intrinsic decrease of the U–Zr matrix conductivity with temperature dominates the overall trend.

IV. Pore connectivity and permeability analyses reveal that the FCCI region maintains dense, highly interconnected networks despite moderate porosity fractions. These networks act as high-diffusivity channels, enabling rapid fission gas venting and accelerating lanthanide delivery to the cladding.

V. Effective thermal conductivity modeling demonstrates that isolated pores degrade conductivity smoothly, while sodium-logged interconnected porosity partially mitigates conductivity loss. Sodium infiltration reduces the performance penalty of high porosity, especially in edge and FCCI regions, but also intensifies FCCI kinetics by enhancing transport.

VI. FCCI progression is governed not only by chemical affinity but also by microstructural topology. Radial pore alignment, short inter-pore distances, and sodium-assisted connectivity create anisotropic diffusion fronts that explain the observed waviness and heterogeneity of the reaction zone.

VII. Overall, these results highlight that porosity topology—not merely volume fraction—controls fuel thermal performance and degradation pathways. Predictive models of metallic fuel must therefore incorporate connectivity-aware transport parameters to capture the interplay between porosity, sodium bonding, and FCCI.

CRediT authorship contribution statement

Anthony A. Harrup: Writing – review & editing, Writing – original draft, Visualization, Software, Methodology, Investigation, Formal analysis, Data curation. **Riley Moeykens:** Writing – review & editing, Methodology, Investigation, Data curation. **Michael Drakopoulos:** Writing – review & editing, Validation, Methodology, Formal analysis, Data curation. **Nghia T. Vo:** Writing – review & editing, Validation, Software, Methodology, Formal analysis, Data curation. **Jana Howard:** Writing – review & editing, Visualization, Formal analysis, Data curation. **Colby B. Jensen:** Writing – review & editing, Resources, Project administration, Funding acquisition. **Tiankai Yao:** Writing – review & editing, Validation, Resources, Project administration, Investigation, Funding acquisition. **Ericmoore Jossou:** Writing – review & editing, Validation, Supervision, Resources, Project administration, Investigation, Funding acquisition, Conceptualization.

Declaration of competing interest

The authors declare that they have no known competing financial interests or personal relationships that could have appeared to influence the work reported in this paper.

Acknowledgments

This work was funded by the Nuclear Energy University Program with award No. DE-NE0009491. This research used resources 27-ID (HEX) of the National Synchrotron Light Source II, a U.S. Department of Energy Office of Science User Facility operated for the DOE Office of Science by Brookhaven National Laboratory under contract No. DE-SC0023462. The sample preparation was carried out at Idaho National Laboratory through the Rapid Turnaround Award (24-4985), which is part of the Nuclear Science User Facilities. E.J. acknowledges the support from the John Hardwick Career Development Chair. The authors would like to acknowledge the staff of the Irradiated Materials Characterization Laboratory (IMCL) at INL for their effort in handling, preparing, and transferring of the samples used in this work.

Appendix: Models used

This appendix summarizes the effective medium models and correlations employed to evaluate the thermal conductivity of porous U–Zr fuel with partially sodium-filled porosity.

A.1 Pore-phase conductivity

The pore medium conductivity is defined as a linear mixture of air and sodium:

$$k_{\text{pore}}(f_{\text{Na}}, T) \;=\; (1 - f_{\text{Na}})\, k_{\text{air}}(T) \;+\; f_{\text{Na}}\, k_{\text{Na}}(T),$$

where f_{Na} is the fraction of porosity infiltrated by sodium.

A.2 Maxwell–Eucken model

For spherical pores embedded in a continuous matrix, the effective conductivity is

$$k_{\text{eff}}^{\text{ME}}(\phi, T) \;=\; k_{\text{solid}}(T)\, \frac{\left(k_{\text{pore}} + 2k_{\text{solid}}\right) - 2\phi\,(k_{\text{solid}} - k_{\text{pore}})}{\left(k_{\text{pore}} + 2k_{\text{solid}}\right) + \phi\,(k_{\text{solid}} - k_{\text{pore}})}.$$

A.3 Bruggeman effective medium theory

The symmetric effective medium approximation satisfies

$$(1 - \phi)\, \frac{k_{\text{solid}}(T) - k_{\text{eff}}^{\text{BRG}}}{k_{\text{solid}}(T) + 2\, k_{\text{eff}}^{\text{BRG}}} \;+\; \phi\, \frac{k_{\text{pore}} - k_{\text{eff}}^{\text{BRG}}}{k_{\text{pore}} + 2\, k_{\text{eff}}^{\text{BRG}}} \;=\; 0.$$

A.4 Percolation reference model

To represent loss of connectivity at high porosity, a percolation model is adopted:

$$k_{\text{eff}}^{\text{perc}}(\phi, T) \;=\; \begin{cases} k_{\text{solid}}(T)\, \left(1 - \dfrac{\phi}{\phi_{\text{c}}}\right)^{t}, & \phi < \phi_{\text{c}}, \\ 0, & \phi \geq \phi_{\text{c}}, \end{cases}$$

with $\phi_{\text{c}} \approx 0.8$ with an exponent $t \sim 2.0$.

A.5 Material correlations

The sodium thermal conductivity is evaluated from a temperature-dependent polynomial fit [43]

$$k_{\text{Na}}(T_{^\circ\text{C}}) = a_0 + a_1 T + a_2 T^2,$$

while the air conductivity is approximated by [43]

$$k_{\text{air}}(T_{^\circ\text{C}}) = b_0 + b_1 T + b_2 T^2.$$

A.6 Karahan-style corrected fuel conductivity

The dense fuel conductivity is corrected for Zr content and porosity/sodium logging as follows [43]:

$$k_f(\phi, T) = k_0(T)\; F_{\text{Zr}}(W_{\text{Zr}})\; P_{\text{c}}(\phi, f_{\text{Na}}),$$

where $k_0(T)$ is the base U–Zr conductivity, F_{Zr} accounts for Zr fraction, and $P_c(\phi, f_{\text{Na}})$ is a porosity/logging correction.

Data availability

Data will be made available on request.

References

[1] R. Pahl, D. Porter, D. Crawford, L. Walters, Irradiation behavior of metallic fast reactor fuels, J. Nucl. Mater. 188 (1992) 3–9, http://dx.doi.org/10.1016/0022-3115(92)90447-S, URL https://www.sciencedirect.com/science/article/pii/002231159290447S.

[2] A.L. Pitner, R.B. Baker, Metal fuel test program in the FFTF, Tech. rep., 1993.

[3] D. Salvato, X. Liu, D.J. Murray, K.M. Paaren, F. Xu, T. Pavlov, M.T. Benson, L. Capriotti, T. Yao, Transmission electron microscopy study of a high burnup U-10zr metallic fuel, J. Nucl. Mater. 570 (2022) 153963, http://dx.doi.org/10.1016/j.jnucmat.2022.153963, URL https://www.elsevier.com/open-access/userlicense/1.0/.

[4] D. Salvato, K.M. Paaren, J.A. Hirschhorn, L.K. Aagesen, F. Xu, F.G. Di Lemma, L. Capriotti, T. Yao, The effect of temperature and burnup on U-10zr metallic fuel chemical interaction with HT-9: A SEM-eds study, J. Nucl. Mater. 591 (2024) http://dx.doi.org/10.1016/j.jnucmat.2024.154928.

[5] T. Yao, L. Capriotti, J.M. Harp, X. Liu, Y. Wang, F. Teng, D.J. Murray, A.J. Winston, J. Gan, M.T. Benson, L. He, α -u and ω -UZr2 in neutron irradiated U-10zr annular metallic fuel, J. Nucl. Mater. 542 (2020) http://dx.doi.org/10.1016/j.jnucmat.2020.152536.

[6] K.H. Kim, S.J. Oh, S.K. Kim, C.T. Lee, C.B. Lee, Microstructural characterization of U-Zr alloy fuel slugs for sodium-cooled fast reactor, in: Surface and Interface Analysis, 44, John Wiley and Sons Ltd, 2012, pp. 1515–1518, http://dx.doi.org/10.1002/sia.4989.

[7] J. Thomas, A.F. Bengoa, S.T. Nori, R. Ren, P. Kenesei, J. Almer, J. Hunter, J. Harp, M.A. Okuniewski, The application of synchrotron micro-computed tomography to characterize the three-dimensional microstructure in irradiated nuclear fuel, J. Nucl. Mater. 537 (2020) http://dx.doi.org/10.1016/j.jnucmat.2020.152161.

[8] D.E. Janney, S.L. Hayes, Experimentally known properties of U-10zr alloys: A critical review, Nucl. Technol. 203 (2018) 109–128, http://dx.doi.org/10.1080/00295450.2018.1435137.

[9] S. Shah, A. Kamboj, K. Wright, D. Salvato, A. Pradhan, D.J. Murray, L. Capriotti, T. Yao, M.N. Bachhav, High resolution microstructural, chemical studies and localized burnup analysis in an irradiated U10zr metallic fuel, Mater. Charact. 228 (2025) 115438, http://dx.doi.org/10.1016/j.matchar.2025.115438, URL https://www.sciencedirect.com/science/article/pii/S1044580325007272.

[10] Q. Zou, F. Lv, Z. Chen, Q. Li, J. Zhao, Q. Ran, Q. Li, Effect of initial fracture angle on the failure pattern and gas flow channel of sandstone under multistage loading, J. Rock Mech. Geotech. Eng. (2025) http://dx.doi.org/10.1016/j.jrmge.2025.12.017.

[11] Q. Zou, Z. Chen, J. Zhan, C. Chen, S. Gao, F. Kong, X. Xia, Morphological evolution and flow conduction characteristics of fracture channels in fractured sandstone under cyclic loading and unloading, Int. J. Min. Sci. Technol. 33 (2023) 1527–1540, http://dx.doi.org/10.1016/j.ijmst.2023.11.003.

[12] E. Plancher, P. Gravier, E. Chauvet, J.J. Blandin, E. Boller, G. Martin, L. Salvo, P. Lhuissier, Tracking pores during solidification of a Ni-based superalloy using 4D synchrotron microtomography, Acta Mater. 181 (2019) 1–9, http://dx.doi.org/10.1016/j.actamat.2019.09.040.

[13] T. Yao, M. Bachhav, F.G. Di Lemma, F. Xu, F. Teng, D.J. Murray, M.T. Benson, L. Capriotti, The advanced characterization, post-irradiation examination, and materials informatics for the development of ultra high-burnup annular U-10zr metallic fuel, Front. Nucl. Eng. 1 (2022) http://dx.doi.org/10.3389/fnuen.2022.1050262.

[14] W.J. Carmack, H.M. Chichester, D.L. Porter, D.W. Wootan, Metallography and fuel cladding chemical interaction in fast flux test facility irradiated metallic U-10zr MFF-3 and MFF-5 fuel pins, J. Nucl. Mater. 473 (2016) 167–177, http://dx.doi.org/10.1016/j.jnucmat.2016.02.019.

[15] J.M. Harp, D.L. Porter, B.D. Miller, T.L. Trowbridge, W.J. Carmack, Scanning electron microscopy examination of a fast flux test facility irradiated U-10zr fuel cross section clad with HT-9, J. Nucl. Mater. 494 (2017) 227–239, http://dx.doi.org/10.1016/j.jnucmat.2017.07.040.

[16] M. Drakopoulos, Z. Zhong, N. Vo, A. Broadbent, M. Lucas, HEX: A new high energy beamline at NSLS-II, Synchrotron Radiat. News 37 (1) (2024) 50–51, http://dx.doi.org/10.1080/08940886.2024.2312071.

[17] N.T. Vo, R.C. Atwood, M. Drakopoulos, T. Connolley, Data processing methods and data acquisition for samples larger than the field of view in parallel-beam tomography, Opt. Express 29 (12) (2021) 17849–17874, http://dx.doi.org/10.1364/OE.418448, URL https://opg.optica.org/oe/abstract.cfm?URI=oe-29-12-17849.

[18] N.T. Vo, R.C. Atwood, M. Drakopoulos, Superior techniques for eliminating ring artifacts in X-ray micro-tomography, Opt. Express 26 (22) (2018) 28396–28412, http://dx.doi.org/10.1364/OE.26.028396, URL https://opg.optica.org/oe/abstract.cfm?URI=oe-26-22-28396.

[19] S. Berg, D. Kutra, T. Kroeger, C.N. Straehle, B.X. Kausler, C. Haubold, M. Schiegg, J. Ales, T. Beier, M. Rudy, K. Eren, J.I. Cervantes, B. Xu, F. Beuttenmueller, A. Wolny, C. Zhang, U. Koethe, F.A. Hamprecht, A. Kreshuk, Ilastik: interactive machine learning for (bio)image analysis, Nature Methods 16 (2019) 1226–1232, http://dx.doi.org/10.1038/s41592-019-0582-9.

[20] V. Boulos, V. Fristot, D. Houzet, L. Salvo, P. Lhuissier, Investigating performance variations of an optimized GPU-ported granulometry algorithm, in: P.S.C.K. T. Papatheodorou (Ed.), Euro-Par 2012: Parallel Processing, Springer, Rhodes, Greece, 2012, pp. 415–426.

[21] W.E. Lorensen, H.E. Cline, Marching cubes: a high resolution 3D surface construction algorithm., Comput. Graph. 1987 (1998) 347–353, http://dx.doi.org/10.1145/280811.281026.

[22] H. Wang, F. Xu, L. Cai, D. Salvato, F.G. Di Lemma, L. Capriotti, T. Yao, M. Xian, A fine pore-preserved deep neural network for porosity analytics of a high burnup U-10zr metallic fuel, Sci. Rep. 13 (2023) http://dx.doi.org/10.1038/s41598-023-48800-3.

[23] Y. Tang, F. Xu, S. Sun, D. Salvato, F.G. Di Lemma, M. Xian, D.J. Murray, C. Judge, L. Capriotti, T. Yao, Segmentation and classification of fission as pores in reactor iirradiated annular u[sbnd]10zr metallic fuel using machine learning models, Mater. Charact. 215 (2024) http://dx.doi.org/10.1016/j.matchar.2024.114061.

[24] D. Yun, A.M. Yacout, M. Stan, T.H. Bauer, A.E. Wright, Simulation of the impact of 3-D porosity distribution in metallic U-10zr fuels, J. Nucl. Mater. 448 (2014) 129–138, http://dx.doi.org/10.1016/j.jnucmat.2014.02.002.

[25] A.V. Gribok, F.G. Di Lemma, J. Fay, D.L. Porter, K.M. Paaren, L. Capriotti, Qualification and quantification of porosity at the top of the fuel pins in metallic fuels using image processing, Energies 17 (2024) http://dx.doi.org/10.3390/en17091990.

[26] A.K. Gupta, B.K. Saxena, S.N. Tiwari, S.L. Malhotra, Pore formation in cast metals and alloys, J. Mater. Sci. 27 (3) (1992) 853–862.

[27] F.A. Nichols, Transport phenomena in nuclear fuels under severe temperature gradients, J. Nucl. Mater. 84 (1979) 1–25.

[28] H. Fang, C.D. Versteylen, S. Zhang, Y. Yang, P. Cloetens, D. Ngan-Tillard, E. Brück, S. van der Zwaag, N.H. van Dijk, Autonomous filling of creep cavities in fe-au alloys studied by synchrotron X-ray nano-tomography, Acta Mater. 121 (2016) 352–364, http://dx.doi.org/10.1016/j.actamat.2016.09.023.

[29] G. Bozzolo, H.O. Mosca, A.M. Yacout, G.L. Hofman, Lanthanides migration in U-zr based nuclear fuels, 407, (ISSN: 00223115) 2010, pp. 228–231, http://dx.doi.org/10.1016/j.jnucmat.2010.10.001,

[30] J.A. Hirschhorn, L.K. Aagesen, C. Jiang, G.L. Beausoleil, Development and preliminary validation of a mechanistic multiscale model for fuel-cladding chemical interaction in metallic nuclear fuels, Nucl. Eng. Des. 432 (2025) http://dx.doi.org/10.1016/j.nucengdes.2024.113811.

[31] D. Stauffer, A. Aharony, Introduction To Percolation Theory, second ed., Taylor & Francis, 1992, http://dx.doi.org/10.1201/9781315274386, [Accessed 25-09-2025].

[32] F.G. Di Lemma, T. Yao, D. Salvato, L. Capriotti, F. Teng, A.M. Jokisaari, B.W. Beeler, Y. Wang, C.J. Jensen, Microstructural and phase changes in alpha uranium investigated via in-situ studies and molecular dynamics, J. Nucl. Mater. 577 (2023) 154341, http://dx.doi.org/10.1016/J.JNUCMAT.2023.154341.

[33] A.C. Bagchi, G.J. Prasad, K.B. Khan, R.P. Singh, A study on zirconium rich uranium-zirconium alloys, Trans. Indian Inst. Met. 67 (2014) 123–130, http://dx.doi.org/10.1007/s12666-013-0326-y.

[34] L. Leibowitz, R.A. Blomquist, A.D. Pelton, Thermodynamics Of The Uranium-Zirconium System *, Tech. rep., 167, 1989, pp. 76–77.

[35] A.A. Galahom, M.A. Abdel-Rahman, M.Y. Mohsen, A. Hakamy, Investigation of the possibility of using a uranium–zirconium metal alloy as a fuel for nuclear power plant AP-1000, Nucl. Eng. Des. 406 (2023) http://dx.doi.org/10.1016/j.nucengdes.2023.112257.

[36] R. Khanal, N. Ayers, N. Jerred, M.T. Benson, R.D. Mariani, I. Charit, S. Choudhury, Role of zirconium in neodymium-dopants interactions within uranium-based metallic fuels, Nucl. Mater. Energy 26 (2021) http://dx.doi.org/10.1016/j.nme.2021.100912.

[37] X. Liu, L. Capriotti, T. Yao, J.M. Harp, M.T. Benson, Y. Wang, F. Teng, L. He, Fuel-cladding chemical interaction of a prototype annular U-10zr fuel with fe-12cr ferritic/martensitic HT-9 cladding, J. Nucl. Mater. 544 (2021) http://dx.doi.org/10.1016/j.jnucmat.2020.152588.

[38] H.E. Ragnauth, The Properties of Uranium-Zirconium Nuclear Fuels and Methods for Improving Burnup Capability (Ph.D. thesis), University of Manchester, 2021.

[39] L. Capriotti, F. Di Lemma, D. Salvato, F. Xu, Y. Tang, K.M. Paaren, A.L. Swearingen, C.B. Jensen, Y. Wang, D.L. Porter, An integrated approach to examine fuel-cladding chemical interaction in HT9/u-10zr metallic fast reactor fuels: Coupling machine learning with electron microscopy and local mechanical properties analysis, J. Nucl. Mater. 616 (2025) http://dx.doi.org/10.1016/j.jnucmat.2025.156092.

[40] W. Chen, X.M. Bai, Temperature and composition dependent thermal conductivity model for U-zr alloys, J. Nucl. Mater. 507 (2018) 360–370, http://dx.doi.org/10.1016/j.jnucmat.2018.05.021.

[41] A. Pradhan, F. Xu, D. Salvato, I. Charit, C. Judge, L. Capriotti, T. Yao, Characterization of fuel cladding chemical interaction on a high burnup U-10zr metallic fuel via electron energy loss spectroscopy enhanced by machine learning, Mater. Charact. 218 (2024) 114524, http://dx.doi.org/10.1016/j.matchar.2024.114524, URL https://www.sciencedirect.com/science/article/pii/S1044580324009057.

[42] A. Eucken, Allgemeine gesetzmäßigkeiten für das wärmeleitvermögen verschiedener stoffarten und aggregatzustände, Forsch. Auf Dem Geb. Des Ingenieurwesens A 11 (1) (1940) 6–20, http://dx.doi.org/10.1007/BF02584103.

[43] A. Karahan, Modeling of Thermo-Mechanical and Irradiation Behavior of Metallic and Oxide Fuels for Sodium Fast Reactors (Ph.D. thesis), Massachusetts Institute of Technology, Cambridge, MA, USA, 2009.